UV Chemistry in the Circumstellar Envelopes of Evolved Stars

MARYAM SABERI

Astronomy and Plasma Physics
Department of Space, Earth and Environment
CHALMERS UNIVERSITY OF TECHNOLOGY
Gothenburg, Sweden 2019

UV Chemistry in the Circumstellar Envelopes of Evolved Stars
MARYAM SABERI

Astronomy and Plasma Physics, Galactic Astrophysics
Department of Space, Earth and Environment
Chalmers University of Technology
SE–412 96 Gothenburg, Sweden
Phone: +46 (0)31–772 1000

Contact information:
Maryam Saberi
Onsala Space Observatory
Chalmers University of Technology
SE–439 92 Onsala, Sweden

Phone: +46 (0)31–772 5546
Fax: +46 (0)31–772 5590
Email: maryam.saberi@chalmers.se

UV Chemistry in the Circumstellar Envelopes of Evolved Stars

MARYAM SABERI
Department of Space, Earth and Environment
Chalmers University of Technology

Abstract

Low- and intermediate-mass stars eject a substantial amount of their material into space during a late phase of stellar evolution, the asymptotic giant branch (AGB) phase. Therefore, they impact the chemistry of the interstellar medium. Due to the intense mass loss, a circumstellar envelope (CSE), rich in gas and dust, forms around the AGB star. Observations of molecular species and dust content in CSEs help us to broaden our knowledge on late phases of stellar evolution, mass-loss processes, the CSE chemistry, and the stellar properties.

For instance, observations of carbon monoxide (CO) have been extensively used to determine the mass-loss rate and the overall CSE properties. Ultraviolet (UV) photodissociation of CO from the interstellar radiation field (ISRF) is the dominant process that determines the CO distribution and extent in CSEs. Therefore, a precise calculation of the CO photodissociation rate is crucial to determine the mass-loss rates. Subsequently, the value adopted for the mass-loss rate in further modelling of the CSEs will affect the abundances derived for all other molecules. Thus, an estimation of the CO photodissociation rate affects the estimates of the amount of all the recycled material. In this thesis, we present the most updated calculations of the depth dependency of the CO photodissociation rate in CSEs using the latest laboratory measurements.

Generally, it is well known that UV radiation impacts the CSE chemistry and the influence of UV radiation from the ISRF has been considered in the models of CSEs. However, there has been little discussion on the impact of internal sources of UV radiation. Recent Galaxy Evolution Explorer observations reveal the presence of strong internal UV radiation for a large sample of AGB stars. The internal UV radiation can originate from stellar chromospheric activity, a hot binary companion, and/or accretion of matter between two stars in a binary system. This thesis seeks to address the impact of both the internal and external sources of UV radiation on the CSE chemistry.

To trace the impact of UV radiation, we present two approaches. First, observations of the main UV photodissociation and photoionization products, such as CI and CII. We present, for the first time, detections of CI around a UV-bright oxygen-rich AGB star, omi Ceti. In the second approach, we investigate the isotopologue ratio of molecules with different photodissociation mechanisms. We expect variations in the isotopologue ratio of molecules that dissociate through lines. However, there should not be any variation by UV radiation in the isotopologue ratio of molecules with continuum dissociation.

Keywords: Astrochemistry – molecular processes – stars: abundances – AGB – binaries – circumstellar matter – chromospheres – ultraviolet

ii

Research contributions

This thesis is based on the work contained in the following papers:

I. *$H^{12}CN$ and $H^{13}CN$ excitation analysis in the circumstellar outflow of R Scl*
M. Saberi, M. Maercker, E. De Beck, W. H. T. Vlemmings, H. Olofsson, and T. Danilovich
Astronomy & Astrophysics, 559, 63 (2017).

II. *Detection of CI line emission towards the oxygen-rich AGB star omi Ceti*
M. Saberi, W. H. T. Vlemmings, E. De Beck, R. Montez, and S. Ramstedt
Astronomy & Astrophysics, 612, 11 (2018).

III. *Photodissociation of CO in the outflow of evolved stars*
M. Saberi, W. H. T. Vlemmings, and E. De Beck
Astronomy & Astrophysics, 625, A81 (2019).

IV. *CO and HCN isotopologue ratios in the outflows of evolved stars*
M. Saberi, W. H. T. Vlemmings, E. De Beck, and H. Olofsson
Manuscript intended for submission to Astronomy & Astrophysics.

Other Publications

I also participated in the following paper not included in the thesis:

- *The UK Infrared Telescope M33 monitoring project - IV. Variable red giant stars across the galactic disc*
A. Javadi, M. Saberi, J. T. van Loon, H. Khosroshahi, N. Golabatooni, M. T. Mirtorabi
Monthly Notices of the Royal Astronomical Society, .447.3973J (2015).

iv

Author's Contributions

Contributions to the appended papers:

- **Paper I:** I performed data reduction of single-dish HCN observations using the XS package. I carried out all the analysis included in the paper, made all the plots, and wrote the paper. All authors actively discussed the methods, analysis and results and revised the manuscript.

- **Paper II:** I applied for the observational data that are used in the paper, performed data reduction using the GILDAS/CLASS package. I conducted all the analysis included in the paper, made all the plots, and wrote the paper. All authors actively discussed the methods, analysis and results and revised the manuscript.

- **Paper III:** I conducted all the simulations included in the paper, made all the plots, and wrote the paper. All authors actively discussed the analysis and results and revised the manuscript.

- **Paper IV:** I performed all the simulations, made all the plots and wrote the paper. All authors discussed the methods, analysis and results.

Acronyms

- **AGB** Asymptotic Giant Branch.

- **ACA** The Atacama Compact Array.

- **ALMA** The Atacama Large Millimeter/submillimeter Array.

- **ALI** Accelerated Lambda Iteration.

- **APEX** The Atacama Pathfinder Experiment.

- **BB** Black body.

- **C** Carbon.

- **CLASS** Continuum and Line Analysis Single-dish Software.

- **CASA** Common Astronomy Software Application.

- **CNO-cycle** Carbon nitrogen oxygen cycle.

- **CO** Carbon monoxide.

- **CSE** Circumstellar envelope.

- **ESO** The European Southern Observatory.

- **FDU** First dredge-up.

- **GALEX** The Galaxy Evolution Explorer.

- **GHz** Gigahertz.

- **GILDAS** Grenoble Image and Line Data Analysis Software.

- **H** Hydrogen.

- **HB** Horizontal branch.

- **He** Helium.

- **H-R** Herzsprung-Russel.

- **ISM** Interstellar medium.

- **ISRF** Interstellar radiation field.

- **MCP** Monte-Carlo program.

- **MS** Main sequence.

- **NAOJ** The National Astronomical Observatory of Japan.

- **NRAO** The National Radio Astronomy Observatory.

- **PDR** Photon dominated region.

- **PN** Planetary nebula.

- **pp-chain** Proton proton chain.

- **RE** Radiative equilibrium.

- **RGB** Red giant branch.

- **RT** Radiative transfer.

- **SE** Statistical equilibrium.

- **SEPIA** The Swedish-ESO PI receiver for APEX.

- **SDU** Second dredge-up.

- **SHeFI** The Swedish Heterodyne Facility Instrument.

- **SOFIA** The Stratospheric Observatory for Infrared Astronomy.

- **TE** Thermal equilibrium.

- **TP-AGB** Thermally-pulsating asymptotic giant branch.

- **UV** Ultraviolet.

Acknowledgements

First and foremost, I would like to thank my supervisor Wouter Vlemmings, who introduced me to the world of Astrochemistry. Thanks for his continued support and encouragement, valuable guidance, and all stimulating scientific discussions we have had during the past five years. Second, I would like to thank Elvire De Beck for giving me assurance, valuable feedbacks and fruitful discussions and thanks for reading and correcting my texts. I am also very grateful for stimulating scientific discussions with Matthias Maercker, Theo Khouri, and Luis Velilla Prieto. Special thanks to my examiner Hans Olofsson for brilliant comments, suggestions, and expert advice. Many thanks to John Black who helped me to gain a deeper understanding about UV photochemistry. I would also thank Tom Millar and Evelyne Roueff for many fruitful discussions and I am grateful for the time they have spent to guide me through astrochemical models during my visits to Belfast and Paris.

Many thanks to all my colleagues at Onsala Space Observatory and Department of Space, Earth and Environment at Chalmers University of Technology, for making such a friendly and inspiring working environment. A special thanks goes to my office-mate and wonderful friend, Daria, for her continued support and all the good memories. Many thanks to Sandra and Flora for all the good times and their support. I would like to thank all PhD students and Postdocs with whom I have had many valuable memories, in particular, Judit, Boy, Jean Baptiste, Grzegorz, Periklis, Joakim, Jonas, Andri, Iskra, Chia-Jung, Juan, Chiara, Magnus, Franz, Sabine, Niklas, Daniel, Hannah, and Farrukh.

Furthermore, I would like thank all my friends for their companionship in the past few years; in particular, Kamran & Parisa, Fatemeh & Sadegh, Elnaz, Neda & Jonas, Parastoo, Mitra & Johan, Maryam & Behzad, Nastaran & Saeed, Parisa & Mohsen, Atefeh, Sara R., Ehsan, Farhang, Aylin, Houisineh, Faezeh & Zdenek, Laleh, Najmeh, Sara Kh., Zahra, Elaheh & Rojman, Sarah., and Hanieh & Arash.

Last but not least, I would like to thank my parents, Amir Hossein, Majid, Saeedeh & Aydin, Mahin & Amir Abbas, Saeed & Shima, Parmis, and the youngest family member, Kourosh, who brought a lot of happiness to the family. Thanks for your unwavering love, unconditional support and encouragement throughout all my studies.

Maryam

Onsala, July 2019

x

Contents

Chapter 1

Introduction

General references:
*Habing (1996); Habing & Olofsson (2003); Herwig (2005); LeBlanc (2010)*

Stars are the sole creators of a large portion of elements including the essential ones for existence of rocky planets, life in the universe, and the human body. The heavy elements produced in the stellar interior are blown out into space during the last phases of stellar evolution. Figure 1.1 presents the origin of the Solar System elements in the Periodic Table.

A large majority of stars are low- and intermediate-mass $(0.8 - 8 M_\odot{}^1)$ stars. These stars eventually evolve into the Asymptotic Giant Branch (AGB) phase. In the AGB phase, stars eject a large portion of their material into space and consequently impact the chemical composition of galaxies. This intense mass-loss $(10^{-8} - 10^{-4} \ M_\odot \text{yr}^{-1})$ makes them of interest as agents of chemical enrichment in the universe. The main aim of this thesis is to further improve our understanding of the chemical composition of the outflow of AGB stars by considering the impact of UV chemistry.

1.1 Outline

This thesis is organized as follows. I review the fundamental physics of stellar evolution with a focus on AGB stars in the rest of this Chapter. Chapter 2 gives a brief overview of sources of UV radiation that impact the chemistry of the outflows of evolved stars and briefly explains molecular photodissociation

---

[1] $M_\odot = 2 \times 10^{30}$ kg corresponds to the mass of the Sun.
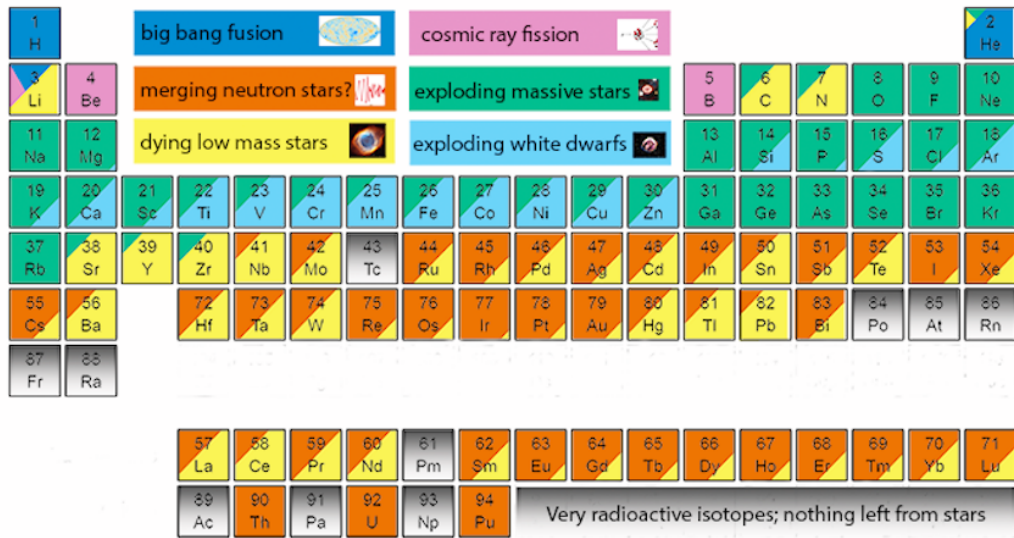
Figure 1.1:   Periodic table showing the origin of the Solar System elements.

mechanisms. Observational data that are used in the appended papers are outlined in Chapter 3. The theory behind radiative transfer and chemical simulations are explained in Chapters 4 and 5, respectively. A short introduction to the appended papers and follow-up ideas are drawn in Chapter 6 and finally Chapter 7 summarizes the results and gives an outline of ongoing work and future plans.

1.2   Stellar Life Cycle

Stars are gravitationally bound spheres of plasma. They are born in giant molecular hydrogen clouds in the interstellar medium. Gravity triggers formation of a protostar by contraction of interstellar clouds. Contraction leads to increasing central density and temperature of the protostar. Once the temperature of the protostar becomes high enough for H nuclear burning in the centre, the protostar begins its life as a main-sequence (MS) star. The nuclear fusion in stars starts with fusion of H to He through the proton-proton chain (pp-chain) and the carbon-nitrogen-oxygen cycle (CNO-cycle). The pp-chain is more prominent in stars with mass $M < 1.3\ M_\odot$ and requires temperature

$T > 4 \times 10^6$ K. The pp-chain occurs through the following pathways:

$$
\text{ppI} \begin{cases} {}^1\text{H} + {}^1\text{H} & \rightarrow & {}^2\text{H} + \text{e}^+ + \nu_\text{e} \\ {}^2\text{H} + {}^1\text{H} & \rightarrow & {}^3\text{He} + \gamma \\ {}^3\text{He} + {}^3\text{He} & \rightarrow & {}^4\text{He} + 2{}^1\text{H} \end{cases}
\tag{1.1}
$$

$$
\text{ppII} \begin{cases} {}^3\text{He} + {}^4\text{He} & \rightarrow & {}^7\text{Be} + \gamma \\ {}^7\text{Be} + \text{e}^- & \rightarrow & {}^7\text{Li} + \nu_\text{e} \\ {}^7\text{Li} + {}^1\text{H} & \rightarrow & 2{}^4\text{He} \end{cases}
\tag{1.2}
$$

$$
\text{ppIII} \begin{cases} {}^7\text{Be} + {}^1\text{H} & \rightarrow & {}^8\text{B} + \gamma \\ {}^8\text{B} & \rightarrow & {}^8\text{Be} + \text{e}^+ + \nu_\text{e} \\ {}^8\text{Be} & \rightarrow & 2{}^4\text{He} \end{cases}
\tag{1.3}
$$
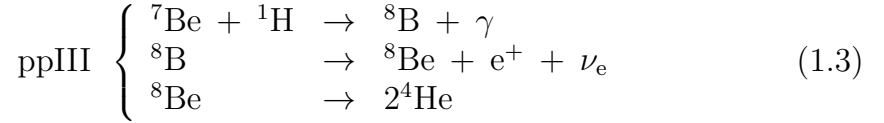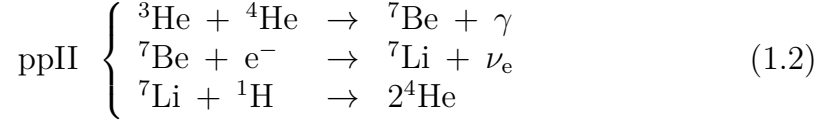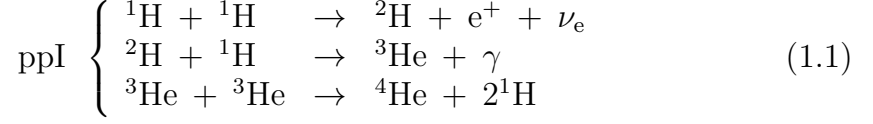
For stars with $M > 1.3\ M_\odot$ the CNO cycle dominates the H fusion. The CNO cycle occurs efficiently at $T > 15 \times 10^6$ K and ${}^{12}\text{C}$ is used as a catalyst as follow:

$$
\text{CNO} - \text{I} \begin{cases} {}^{12}\text{C} + {}^1\text{H} & \rightarrow & {}^{13}\text{N} + \gamma \\ {}^{13}\text{N} & \rightarrow & {}^{13}\text{C} + \text{e}^+ + \nu_\text{e} \\ {}^{13}\text{C} + {}^1\text{H} & \rightarrow & {}^{14}\text{N} + \gamma \\ {}^{14}\text{N} + {}^1\text{H} & \rightarrow & {}^{15}\text{O} + \gamma \\ {}^{15}\text{O} & \rightarrow & {}^{15}\text{N} + \text{e}^+ + \nu_\text{e} \\ {}^{15}\text{N} + {}^1\text{H} & \rightarrow & {}^{12}\text{C} + {}^4\text{He} \end{cases}
\tag{1.4}
$$

$$
\text{CNO} - \text{II} \begin{cases} {}^{15}\text{N} + {}^1\text{H} & \rightarrow & {}^{16}\text{O} + \gamma \\ {}^{16}\text{O} + {}^1\text{H} & \rightarrow & {}^{17}\text{F} + \gamma \\ {}^{17}\text{F} & \rightarrow & {}^{17}\text{O} + \text{e}^+ + \nu_\text{e} \\ {}^{17}\text{O} + {}^1\text{H} & \rightarrow & {}^{14}\text{N} + {}^4\text{He} \end{cases}
\tag{1.5}
$$

$$
\text{CNO} - \text{III} \begin{cases} {}^{17}\text{O} + {}^1\text{H} & \rightarrow & {}^{18}\text{F} + \gamma \\ {}^{18}\text{F} & \rightarrow & {}^{18}\text{O} + \text{e}^+ + \nu_\text{e} \\ {}^{18}\text{O} + {}^1\text{H} & \rightarrow & {}^{15}\text{N} + {}^4\text{He} \end{cases}
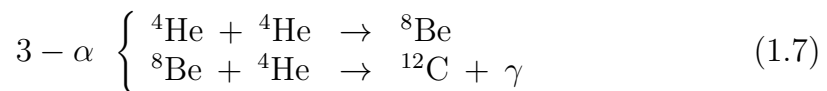\tag{1.6}
$$
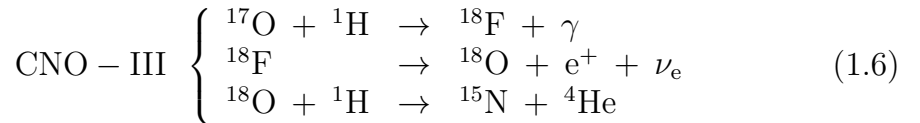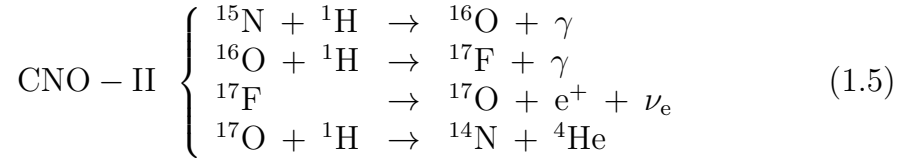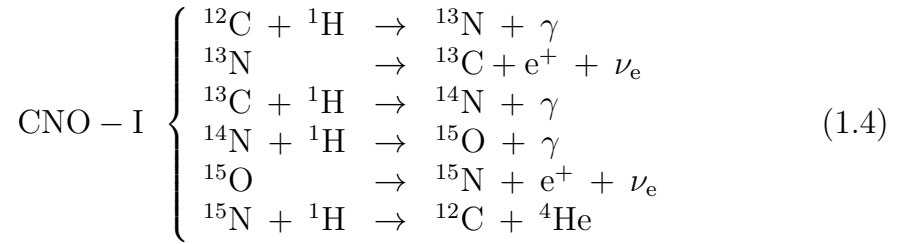
The MS phase is the longest and most stable phase of the stellar evolution. The stellar life time and post-MS evolutionary phases depend on the initial mass of the star. Generally, massive stars evolve quicker than less massive stars. The MS phase lasts for approximately 10^{10} yr for a 1 $M_\odot$ star and 3×10^7 yr for a 8 $M_\odot$ star. Here, we focus on the evolutionary tracks of low- to intermediate-mass $(0.8 - 8 M_\odot)$ stars.

To illustrate the stellar evolutionary phases, it is useful to plot a Herzsprung-Russel (H-R) diagram which shows the relation between surface temperatures and luminosities of stars. These two measurable quantities vary significantly

during the evolution of a given star. Competition between two forces, gravity and pressure due to nuclear fusion reactions, plays a critical role in the stellar evolution, and determines the positions of stars in the H-R diagram. Figure 1.2 presents the evolutionary track of a 1 $M_\odot$ mass star in the H-R diagram and its inner structure at three different phases of evolution. It also highlights positions of zero age MS stars with different initial masses in a diagonal path. High mass stars lie at the top left (high luminosities and high temperatures) and low mass stars are located at the bottom right (low luminosities and low temperatures) of the HR diagram.

Stars in the MS phase are in thermal and hydrostatic equilibrium, meaning that the inward force of gravity is balanced by the outward force of thermal pressure. Eventually most of the hydrogen supply is consumed in the core and the temperature is not high enough for the He burning. Thus, at some point self-gravity overcomes thermal pressure and the core collapse takes place. However, while the nuclear burning stops in the core, hydrogen is still burning in a shell around the inert central region. The He core is continuously fed by the He from the upper shell. The energy produced in the shell-burning causes the expansion of the outer layers. The outer envelope becomes convective. During the expansion, the effective temperature of the star decreases slightly so that the star becomes cooler and redder. The star evolves rapidly towards the red giant branch (RGB) phases. The RGB phase lasts for approximately 10^9 yr for a 1 $M_\odot$ star. At the RGB, the convective envelope reaches down to the inner layers and brings material enriched in ^{4}He, ^{14}N and ^{13}C to the surface. This process is called the first dredge-up (FDU). The FDU happens for all stars in the RGB phase regardless of their initial masses. Eventually the core collapse provides the critical temperature of (10^8K) needed for the He fusion through the triple-alpha (3-α) process as follow:

$$3 - \alpha \begin{cases} ^4\text{He} + {}^4\text{He} & \rightarrow & {}^8\text{Be} \\ ^8\text{Be} + {}^4\text{He} & \rightarrow & {}^{12}\text{C} + \gamma \end{cases} \tag{1.7}$$

For stars with $M \leq 2\ M_\odot$, the electrons in the core become degenerate due to the core contraction. Therefore, the pressure in the core does not obey the ideal gas law, meaning that the temperature can increase without increasing the pressure. This leads to more nuclear energy production in the core. The released energy due to the fusion increases the reaction rate, causing an explosive reaction in the core, called He-core flash. The He-core flash is very short lived and during that the luminosity of the star is greatly increased. The sudden increase in temperature lifts the degeneracy and the star moves downward to the horizontal branch (HB). The hydrostatic equilibrium will be restored again. During the HB phase, the star burns He in its core and H in a shell outside the core. A 1 $M_\odot$ star stays in the HB phase for about 10^8 yr.
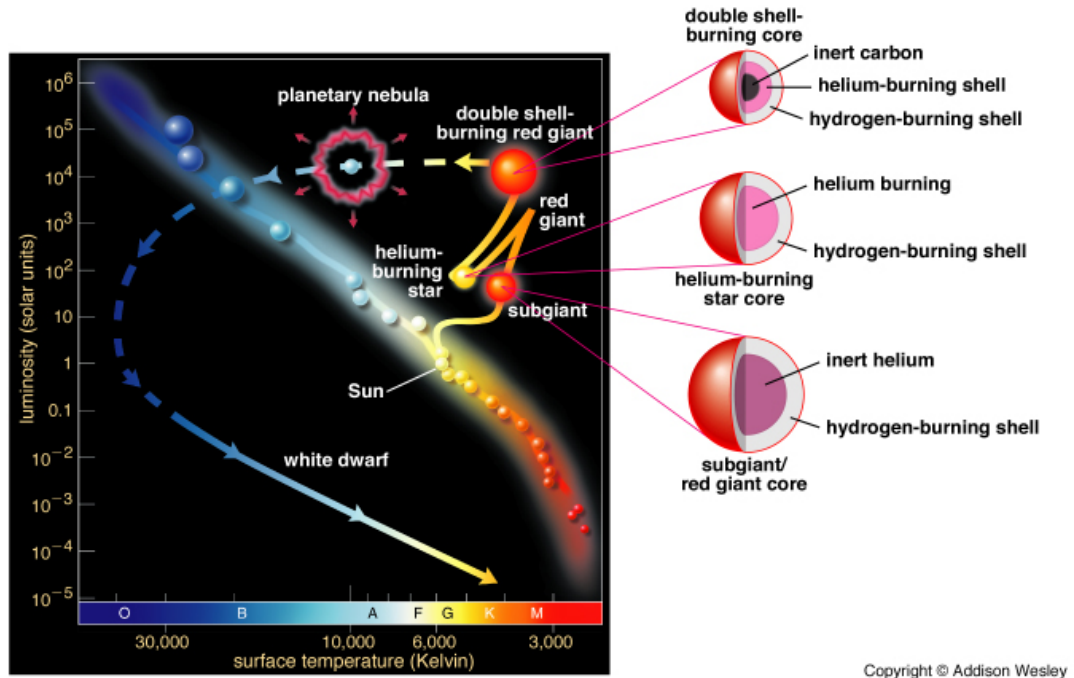
Figure 1.2: Hertzsprung-Russell diagram for a $1 M_\odot$ star.

Eventually most of the He in the core is fused. The released energy due to the He burning expands the outer layers and the star ascends the giant branch for a second time, the asymptotic giant branch (AGB) phase. The star now has a degenerate carbon-oxygen rich core surrounded by two distinct He- and H-burning shells with an intershell zone separating the two and a convective stellar envelope on top which is shown in Fig. 1.3. The luminosity of the AGB star is provided by the two burning shells.

In the early AGB, stars with $M > 4\ M_\odot$ experience a second dredge-up (SDU) event in which the large convective envelope from the stellar surface penetrates down into the dormant H burning shell. Due to the SDU event the outer layer of the AGB star will be enriched with products of the CNO cycle such as ^{4}He, ^{12}C, and ^{14}N. For low-mass stars ($M < 4\ M_\odot$), since convention can not reach below the H shell the SDU does not occur.

The He- and H-shell burning in the AGB phase does not smoothly go forward and are subject to thermal instabilities. The thermal instability of the He shell is due to the high sensitivity of the 3-α reaction on the temperature coupled with the thinness of the shell. Due to the thermal instabilities, the dominant source of stellar luminosity oscillates between the H- and He- burning shells. This leads to the variation of the total luminosity. This is the beginning of the thermally-pulsing AGB (TP-AGB) phase. The
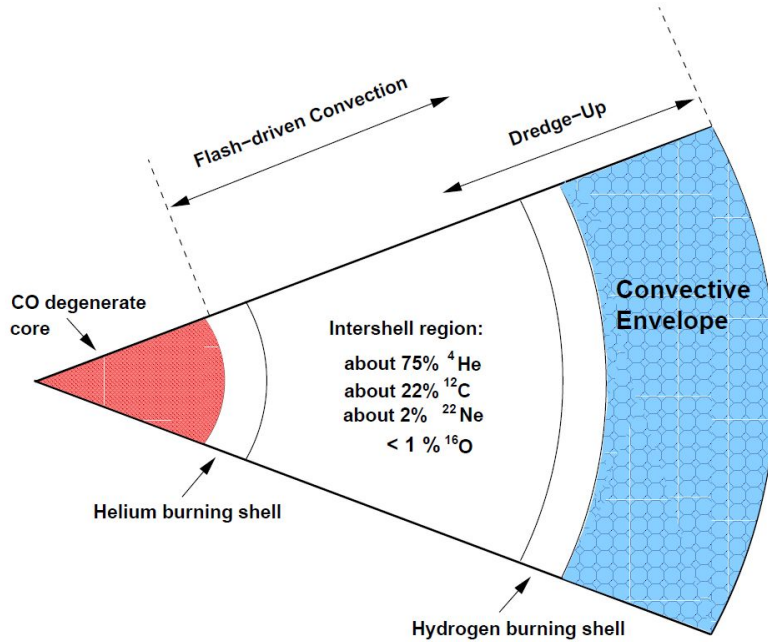
Figure 1.3:   A schematic view of the structure of an AGB star (not to scale), from Karakas et al. (2002).

number of thermal pulses, the time scale between pulses, and the luminosity variations due to thermal pulses depend on the AGB mass. The time-scale between pulses is estimated to be 10^5 yr for a 1 $M_\odot$ star and 10^4 yr for a 4 $M_\odot$ star. Each thermal pules causes large changes in luminosity and mass-loss rate. The thermal pulse events continue until the hydrogen rich convective envelope disappeared by mass loss. The TP-AGB phase typically lasts about 10^6 yr, although the exact time scale again depends on the stellar mass.

During the late AGB phase, a third dredge-up (TDU) event comes along with each thermal pulse for stars with $M > 1.5 \, M_\odot$. We note that this term, TDU, is also used for low-mass stars ($1.5 < M < 4 \, M_\odot$) that did not go through the second dredge-up; in fact all dredge-up events after the thermal pulses are called TDU. This process brings the H- and He-burning products to the surface of the star and changes the surface composition. The C/O ratio increases with each TDU event, leading to evolve the star from an oxygen-rich (C/O<1) to a carbon-rich (C/O>1) AGB star. In addition to the ^{12}C, TDU brings the slow neutron capture process (s-process) elements, the elements heavier than iron which synthesize during the AGB, to the stellar surface. The number of thermal pulses and hence TDU events depends on the mass of the star and mass-loss rate which eventually terminates the AGB phase.

In stars with $M > 4 \, M_\odot$, the temperature at the bottom of the convective envelope becomes very high ($T > 3 \times 10^7$ K) during thermal pulses.

Consequently, the H-burning will occur through the CNO cycle in the the convective envelope, a process known as hot bottom burning (HBB). During HBB, ^{12}C burns to ^{13}C and ^{14}N. HBB prevents massive stars to become C-type AGB stars; instead they become efficient producers of N.

The AGB is the last phase of nuclear burning for low- and intermediate-mass stars since the temperature of the core does not rise enough for carbon burning to occur. This is because of the degeneracy of the C-O core which will be cooled by neutrino emission. This puts an upper limit of $M \sim 8\ M_\odot$ for AGB stars. A $1 M_\odot$ star will stay in the AGB phase for approximately 2×10^7 yr.

When the star reaches the tip of the AGB, the mass loss rate drastically increases (up to $10^{-4} M_\odot$ yr^{-1}) which is called a 'superwind'. Once the mass of the H-rich envelope becomes less than about $0.01 M_\odot$, the envelope shrinks. Consequently, the AGB star horizontally moves in the HR diagram towards higher effective temperatures and that is the beginning of the post-AGB phase or pre-planetary nebulae. Eventually the effective temperature exceeds 30,000 K and the star radiates a strong UV flux which can destroy the dust grains, dissociate the molecules, and finally ionize the gas in the CSE. Part of the CSE consequently becomes ionized (an HII region) and starts radiating in recombination lines. The H-burning shell will be halted once the envelope mass has decreased to $10^{-5}\ M_\odot$ and therefore the luminosity will be decreased. The remnant is called a white dwarf which gets cooler and less luminous, and turns, theoretically, to a black dwarf. A more detailed description of AGB stars and their chemical evolution is presented in the following Section.

1.3   AGB Characteristics

AGB stars are giant ($R_\star \sim 300 R_\odot$[2]) stars with luminosities ranging from $L \sim$ 3000-20000 L$_\odot$[3] and surface temperatures of $T \sim$1800-3000 K. Pulsations of the star yield variability with a period of hundreds of days. AGB stars can be divided into three variability types regarding the amplitude and regularity of the pulsation: high-amplitude regular Mira variable (variability > 2.5 mag in the visual), low-amplitude semi-regular variable (variability ~ 1 mag in visual) and low-amplitude irregular variable. Moreover, helium shell flashes also direct to longer-term variability which may interact with shorter-term variability due to pulsations.

---

[2] $R_\odot = 6.9 \times 10^{10}$ cm corresponds to the solar radius.
[3] $L_\odot = 3.8 \times 10^{26}$ W corresponds to the solar luminosity.

1.3.1   Mass Loss

In the AGB stage, the star loses up to 80% of its initial mass typically at rates of $10^{-8} - 10^{-4} \, M_\odot \, \mathrm{yr}^{-1}$. This makes AGB stars important suppliers of heavy elements and dust to the interstellar medium. The mass-loss characterizes and terminates the evolution on the AGB. The mechanisms driving mass-loss are not completely understood. The most widely accepted theory says that a combined action of pulsations and radiation pressure on dust plays an essential role in steering such strong mass-loss. The idea is that the pulsations induce shock waves in the stellar atmosphere. Induced shock waves elevate the gas particles to larger radii ($1 < R \leq 5R_\star$, where $R_\star$ is the stellar radius) where the temperature is low enough ($T \sim 1500$ K) for the dust formations from gas particles. In this region, the new formed dust grains can be easily accelerated by radiation pressure from stellar luminosity. Even though dust grains only comprise about 1% of the mass of the atmosphere and the rest is in form of molecular gas (mostly H_2), the molecular gas is dragged along with the accelerated dust particles and forms the circumstellar envelope (CSE) around the star. In C-type AGB stars, carbon dust particles form close to the star at $R \sim 2R_\star$ and efficiently lift the molecular gas from photosphere. In M-type AGB stars, alumina dust form at the inner region close to the star ($R < 2R_\star$) and start to drive the mass loss and then at larger radii ($R > 5R_\star$), the silicate dust can be formed and drag the molecular gas along (Millar 2016, and references therein).

During thermal pulses, AGB stars experience short phases (a few hundred years) of intense mass loss ($\sim 10^{-5} M_\odot \mathrm{yr}^{-1}$). These brief episodes of intense mass loss lead to the formation of a geometrically thin detached-shell of gas and/or dust around AGB stars. Figure 1.4 clearly shows the CSE and detached shell of a C-type AGB star, R Scl, in the CO(J=3-2) ALMA observations (Maercker et al. 2012). The spiral pattern observed in the CSE is due to a previously unknown binary companion at a distance of approximately 60 AU from the central star.

1.3.2   CSE Chemistry

The physical conditions and processes dominating the CSE chemistry change as a function of distance from the star in a measurable manner. Figure 1.5 presents a schematic view of the main processes dominating the chemistry in different parts of a CSE. Photospheric or parent species form under thermal equilibrium (TE) conditions in the photosphere. The TE conditions do not hold for the layers above the photosphere due to the passage of stellar pulsations and shocks. This may change the initial molecular setup of the wind by changing the molecular formation paths (e.g. Cherchneff 2006). At
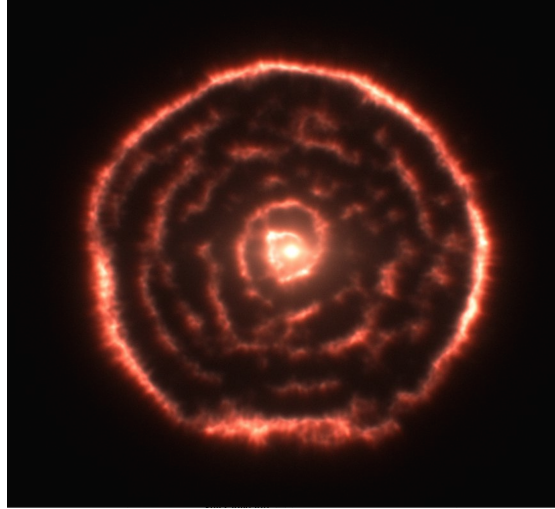
Figure 1.4: ALMA observations of ^{12}CO (J=3-2) towards the AGB star R Scl show the detached-shell and the CSE, Maercker et al. (2012). The spiral pattern in the outflow is due to a binary companion. Image credit: ESO.

larger radii ($R \geq 1R_\star$) the temperature is low enough for dust formation and growth. The photospheric species then can be lifted to larger radii by accelerated dust particles. In the outer CSE where the interstellar UV photons penetrate into the CSE, the photo-chemistry mainly controls the molecular composition and extension. In this region, new molecules can locally form through different chemical and radiative processes induced by cosmic rays and the ISRF.

Generally the molecular content and dust grain types of CSEs are determined by the elemental C/O ratio in the atmosphere. AGB stars can be classified into two main categories of carbon rich C-type (C/O>1) and oxygen rich M-type (C/O<1). The atmosphere of C-type stars are rich in CO and other C-bearing molecules such as C_2, C_2H_2 and HCN, while the M-type stars are rich in CO and other O-bearing molecules such as H_2O and TiO, (e.g. Le Bertre 1997). Table 1.1 shows the most updated list of molecules detected in the CSEs of AGB stars. Observations of dust continuum and molecular emission and absorption lines of CSEs are used to constrain both the stellar properties and the molecular content of the outflows. CO is the most widely used molecule to constrain the CSEs properties such as mass-loss rate, density structure, expansion velocity profile, and kinetic temperature in both C-type and M-type AGB stars. This is because CO is easily detectable and chemically stable therefore its abundance does not significantly vary throughout the CSE. The information extracted from CO radiative transfer modelling and dust continuum modelling will be used to derive the abundance of all other species.
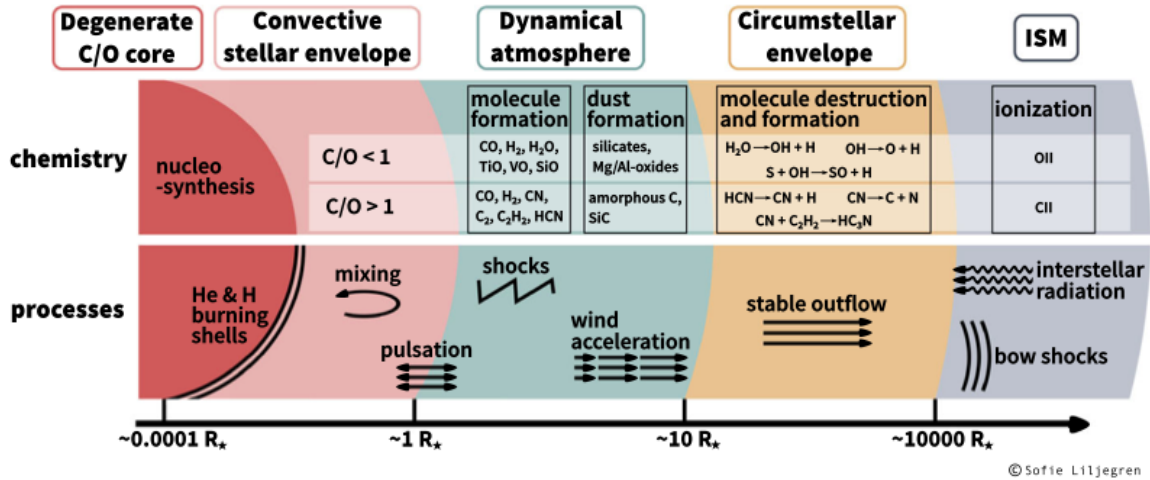
Figure 1.5: A schematic view of an AGB star and its CSE from Höfner & Olofsson (2018). Image credits: S. Liljergen.

1.3.3 Isotopic Ratio

Studying isotopic ratios of evolved stars provides important information on the initial stellar mass, the stellar evolutionary phases, and the chemical enrichment of the interstellar medium (e.g. Karakas & Lattanzio 2014; Justtanont et al. 2015; Höfner & Olofsson 2018). Figure 1.6 outlines different events that alter the isotopic abundances at the stellar surface for different mass stars. As indicated the photospheric $^{12}\text{C}/^{13}\text{C}$ ratio can be a good tracer of the stellar mass, nucleosynthesis, and evolutionary stage.

The advantage of using the isotopic ratios lies in the reliability of the ratios compared to the absolute abundance values, since the ratios are less dependent on the limitations of modelling and observational errors that affect the absolute values.

From observational aspects, direct measurements of elemental photospheric ratios are very challenging and sometimes impossible with current observational techniques. Hence, observations of circumstellar molecules, which possess permanent dipole moments and are thus observable at radio/mm/submm frequencies, are extensively used as tracers of the elemental photospheric ratios. Observations of the circumstellar $^{12}\text{CO}/^{13}\text{CO}$ are widely used to trace the elemental photospheric $^{12}\text{C}/^{13}\text{C}$ ratio in the CSEs (e.g. Groenewegen et al. 1996; Greaves & Holland 1997; Schöier & Olofsson 2000; Milam et al. 2009; Ramstedt & Olofsson 2014). However, discrepancies between the photospheric $^{12}\text{C}/^{13}\text{C}$ and the circumstellar $^{12}\text{CO}/^{13}\text{CO}$ ratios have been observed for a number of AGB stars. This can be explained by considering higher optical depth of ^{12}CO and the sensitivity of the CO fractionation reaction to

Table 1.1: Molecules and ions detected in AGB CSEs.

2 atoms:	OH	HF	C_2	CN	CO	HCl
	SiC	SiN	$AlO^\star$	CP	CS	SiO
	PN	AlF	PO	SO	NaCl	SiS
	AlCl	KCl	NS			
3 atoms:	H_2O	C_2H	HCN	HNC	H_2S	C_3
	CCN	CO_2	HCP	NaCN	MgCN	MgNC
	SiC_2	AlNC	SiCN	SiNC	C_2P	C_2S
	SO_2	KCN	SiCSi	FeCN	CaNC	
4 atoms:	NH_3	C_2H_2	H_2CO	PH_3	$l\text{-}C_3H$	$c\text{-}C_3H$
	HC_2N	H_2CS	C_3N	$MgC_2H^\star$	HMgNC	C_3O
	$c\text{-}SiC_3$	C_3S	$NC_2P^\star$	$l\text{-}H_2C_3$	H_2CO	
5 atoms:	CH_4	CH_2NH	SiH_4	$c\text{-}C_3H_2$	$c\text{-}C_3H_2$	CH_2CN
	C_4H	HC_3N	HC_2NC	HNC_3	C_5	SiC_4
	H_2C_3					
6 atoms:	C_2H_4	CH_3CN	H_2C_4	$SiH_3CN^\star$	C_5H	HC_4N
	C_5N	C_5S	C_4H_2			
$\geq 7 atoms:$	CH_3CCH	CH_2CHCN	C_6H	H_2C_6	HC_5N	C_7H
	C_8H	HC_7N	HC_9N	CH_3SiH_3		
Ions:	CN^-	HCO^+	C_3N^-	C_4H^-	C_5N^-	C_6H^-
	C_8H^-					

Note: * indicates a tentative detection.

temperature. These can lead to variations of the $^{12}CO/^{13}CO$ ratio throughout the CSEs. This indicates that although CO is the best candidate to determine the physical properties of the CSEs, its circumstellar isotopologue ratio may not be the greatest option of tracing the photospheric $^{12}C/^{13}C$ ratio.
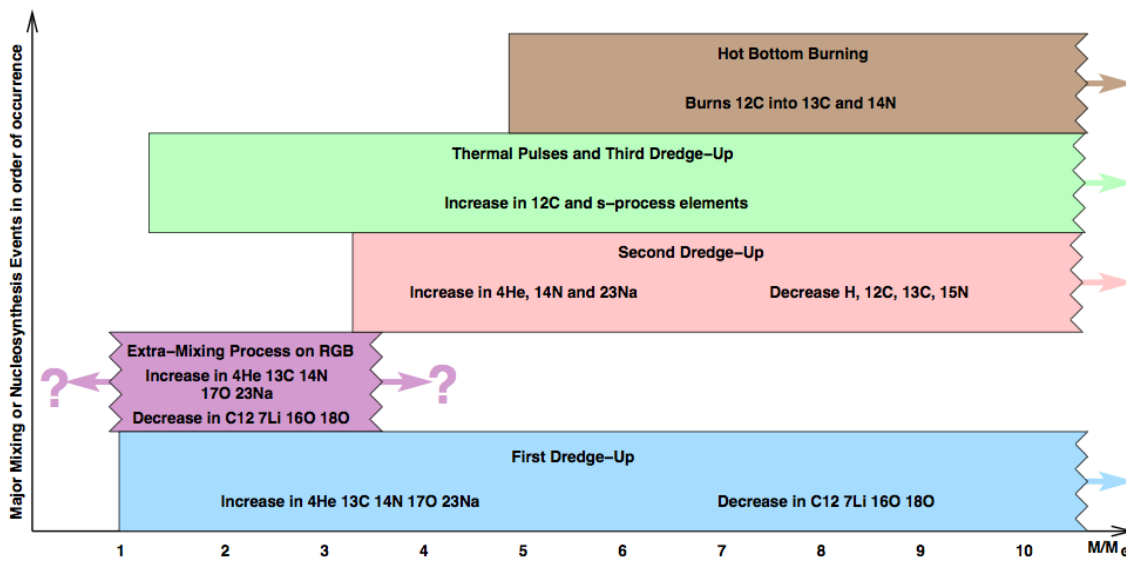
Figure 1.6:   A schematic view of the mass dependence of different events that change the stellar surface composition and isotopic ratio. The lower mass limit depends on the metallicity, the values presented here correspond to solar metallicity Z=0.02. Image from Karakas & Lattanzio (2014).

Chapter 2

UV Chemistry

In this Chapter, I summarize all known sources of UV radiation that can potentially influence the CSE chemistry. I also give a brief overview of the molecular dissociation mechanisms.

2.1 Potential Sources of UV Radiation

Ultraviolet (UV) radiation (100-4000 Å) controls the photodissociation and photoionization of molecular and atomic species in the CSEs around AGB stars. UV photodissociation of the molecular gas is thought to be dominated by the interstellar radiation field (ISRF) while the star is on the AGB phase. AGB stars have low surface temperatures of ~1800-3000 K, therefore their intrinsic UV radiation is not expected to heavily affect the CSE chemistry. Van de Sande & Millar (2019) show that including a source of UV radiation in the form of a black body (BB) with effective temperature of 2100-2600 K only influences the chemistry of CSEs of low mass-loss AGB stars with clumpy envelopes.

Recent Galaxy Evolution Explorer (GALEX) observations reveal the presence of strong internal UV radiation from 179 AGB star which covers $\sim 57\%$ of the observed sample of AGB stars (Montez et al. 2017). This indicates the existence of a strong internal source of UV-radiation which has not been considered before in models of AGB stars and their outflows. Figure 2.1 shows the UV spectra from two AGB stars observed by GALEX from Montez et al. (2017). For a single AGB star, the intense internal UV radiation can be due to stellar chromospheric activity. In binary systems, in addition to the stellar chromospheric activity, a hot binary companion, and/or accretion of material between the AGB star and its companion can generate UV radiation.
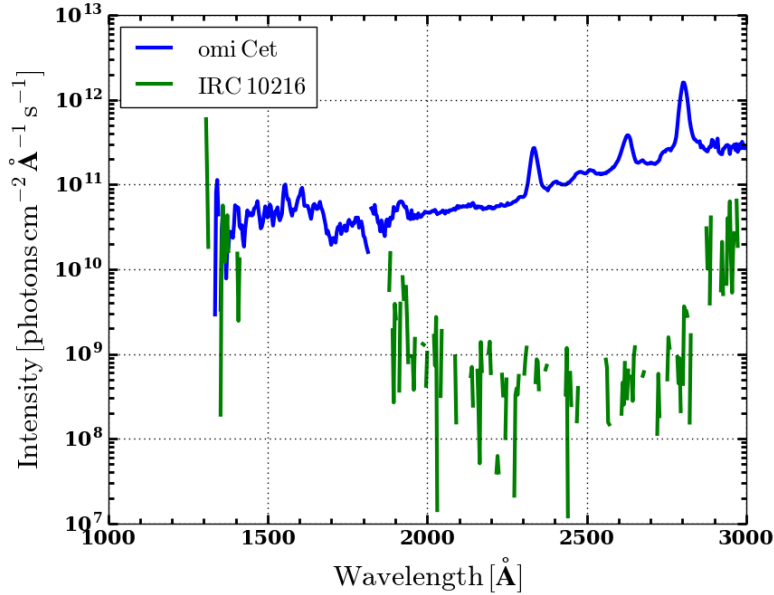
Figure 2.1: GALEX grism UV spectroscopy towards two AGB stars IRC+10216 and *o*mi Cet clearly shows the presence of strong internal UV radiation. The data are taken from Montez et al. (2017).

2.1.1 External UV Radiation - ISRF

The most widely used ISRF in models of AGB stars is the one presented by Draine (1978). He fits an analytical formula to the UV observations in the wavelength range $\sim 900 - 2000$Å in the solar neighborhood. One has to be careful in applying the Draine ISRF in models since the position of a given source in space influences the intensity of the ISRF. The main ISRF UV sources, hot O and B type stars, are not isotropically distributed in the Galaxy, therefore the ISRF source function depends on the spatial position of the source in the Galaxy (Murthy & Henry 1995). McDonald et al. (2015) have shown that the ISRF is significantly higher in globular clusters than the standard commonly used ISRF. On the other hand, sources that are located above the Galactic plane e.g. IRC+10216 are possibly exposed to a weaker ISRF. The strength of the ISRF may significantly affect the chemistry of the outer CSE. In paper III, we have shown how this affects the CO photodissociation radius.

In addition to the strength of the local ISRF, penetration of the ISRF into the CSE material depends also on a number of CSE properties such as geometry, clumpiness, and dust composition.

The radially expanding CSEs around AGB stars can be approximated by a spherically-symmetric geometry. We have to remind that photon dominated region (PDR) models that are developed for studying interstellar clouds usually assume a plane-parallel geometry. This kind of codes are not appropriate for CSE modelling unless one only is interested in modelling the outer CSE where the velocity has already reached the terminal velocity.

Several observations have shown that CSEs have clumpy structures both on small and large scales (e.g. Chapman et al. 1994; Guélin et al. 1997; Weigelt et al. 1998; Fong et al. 2003; Leão et al. 2006). The degree of clumpiness (or volume filling factor) in the winds of AGB stars is not well characterised. A clumpy circumstellar medium allows the interstellar UV-radiation to penetrate deeper into the CSE compared to a uniform CSE with the same average column density (Meixner et al. 1992). This may also impact the chemical composition (e.g. Lee 1984; Agúndez et al. 2010; Van de Sande et al. 2018).

Goicoechea & Le Bourlot (2007) show that the FUV penetration into molecular clouds can heavily depend on the dust albedo and anisotropy of the scattered radiation. Consequently, the grain properties and growth must be taken into account. These are different from source to source and even within the same source. They show that the assumption of uniform dust properties and average extinction curves can be a crude approximation to determine the scattering properties for the ISM. This might affect the modelling results of molecules which are mostly radiatively excited. In case of AGB stars, the exact dust properties in CSEs have not been constrained. Future studies require a more precise treatment of the dust properties in both chemical and radiative transfer modelling of AGB stars but this is beyond the scope of this work.

2.1.2 Internal UV Radiation - Chromospheric Activity

The chromosphere is a layer of plasma overlying the photosphere where the temperature goes from ~ 4000 to 25000 K and the density drops quickly. In the stellar photosphere in radiative equilibrium (RE) condition, energy transport through the plasma is purely by radiation. Unlike the photosphere, the chromosphere is not in RE. Thus, a non-thermal mechanism of energy transport must be present. Magnetic and acoustic heating are potential sources for heating the stellar chromospheres.

Previous studies of UV-spectra indicate the presence of a chromosphere in the outer atmosphere of giant stars (e.g. Hartmann et al. 1982; Querci & Querci 1985; Johnson et al. 1986; Eaton & Johnson 1988; Judge & Stencel 1991; Schrijver 1995; Carpenter et al. 1997). Several emission features of high temperature ionized species such as FeII, CaII, and CII from cool stars are

the observational tracers of the stellar chromospheres. Moreover, emission lines such as the CaII, H and K lines are a sure sign of departure from RE condition, and thus of chromospheric origin emission.

2.1.3   Internal UV Radiation - Binary Companions

Binarity has been offered as a possibility to explain the shape of planetary nebulae (PNe) or asymmetries in the CSEs of AGB stars. However, the rate of binarity in evolved stars is not precisely known. The discovery of companions is more straightforward when the companion is hot such as a white dwarf, but the detection of low- to intermediate MS companions is not straightforward. Sahai et al. (2008) and Ortiz & Guerrero (2016) report the detection of UV-radiation for a sample of AGB stars, interpreted as arising from a hot embedded companion. Although it should be noted that they have not considered the possibility of the UV radiation by the AGB star itself.

Figure 2.2 indicates the UV intensity of the Draine ISRF, the Sun, and three BB sources with different effective temperatures. A first, simple approach to adopt an internal UV field from a binary companion into chemical models of AGB CSEs would be to consider a hot BB source.

2.2   Molecular Photodissociation by UV Radiation

Photodissociation is a chemical process in which a molecule breaks apart by absorbing light. Molecular photodissociation can be dominated by either direct or indirect photodissociation mechanisms depending on the structure of the molecule. Figure 2.3 schematically illustrates all types of photodissociation processes.

In *direct photodissociation*, a molecule is excited from the ground electronic state to a higher energy electronic state, that is repulsive with respect to the nuclear coordinate, by absorbing a single photon. In this process, since spontaneous emission back to the ground state is comparatively slow (typical Einstein-A coefficients of 10^9 s^{-1} compared with dissociation times of 10^{13} s^{-1}), all of the absorptions lead to molecular dissociation. Therefore the photodissociation cross section is continuous as a function of photon energy. The photodissociation rate in s^{-1} by continuous absorption can be expressed by

$$k_{\mathrm{pd}}^{\mathrm{cont}} = \int \sigma(\lambda) I(\lambda) d(\lambda), \tag{2.1}$$
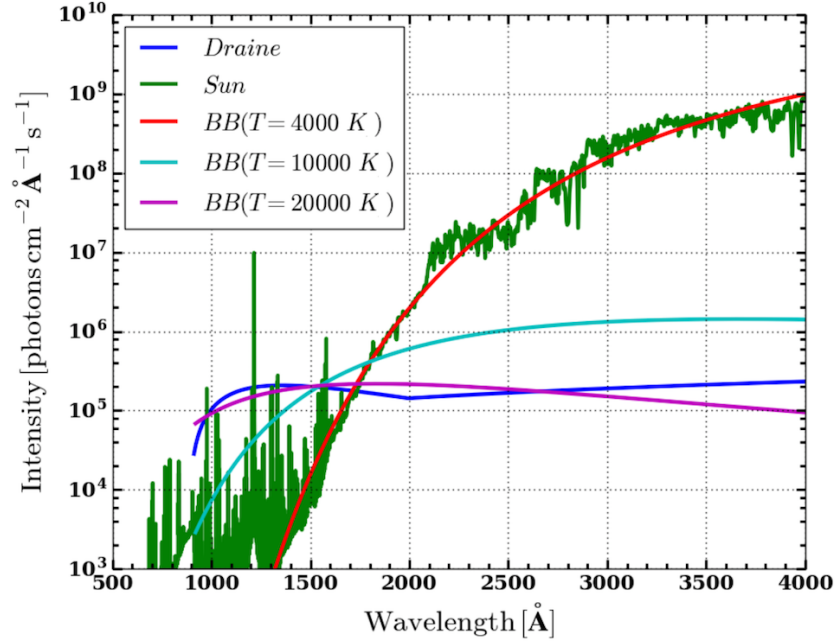
Figure 2.2: Comparison between UV radiation from the ISRF from Draine, the Sun, and black bodies with three different effective temperatures. All radiation fields have been scaled to agree with the integrated energy-intensity of the Draine (1978) radiation field between 91.2 and 200 nm. The data are from `https://home.strw.leidenuniv.nl/~ewine/photo/index.php?file=radiation_fields.php`

where σ is the photodissociation cross section in cm^2 and I is the mean intensity of the radiation in photons $cm^{-2}\,s^{-1}\,Å^{-1}$ as a function of wavelength λ in Å.

Indirect photodissociation can be classified into two categories, predissociation and spontaneous radiative dissociation. In *predissociation*, the molecule is initially excited to a bound electronic state and subsequently interacts non-radiatively with a nearby repulsive electronic state. In this case, the photodissociation cross section contains a series of discrete peaks. The peaks are proportional to the product of the oscillator strength of the initial absorption and the dissociation efficiency of the level involved. In the case that the excited bound state is not predissociated, *spontaneous radiative dissociation* can still be effective by emission of photons into the continuum of a lower repulsive state or the vibrational continuum of the ground electronic state. This photodissociation cross section likewise involves a series of discrete peaks (Fig. 2.3).

The photodissociation rate for indirect processes of predissociation and spontaneous radiative dissociation for the rate of dissociation by absorption
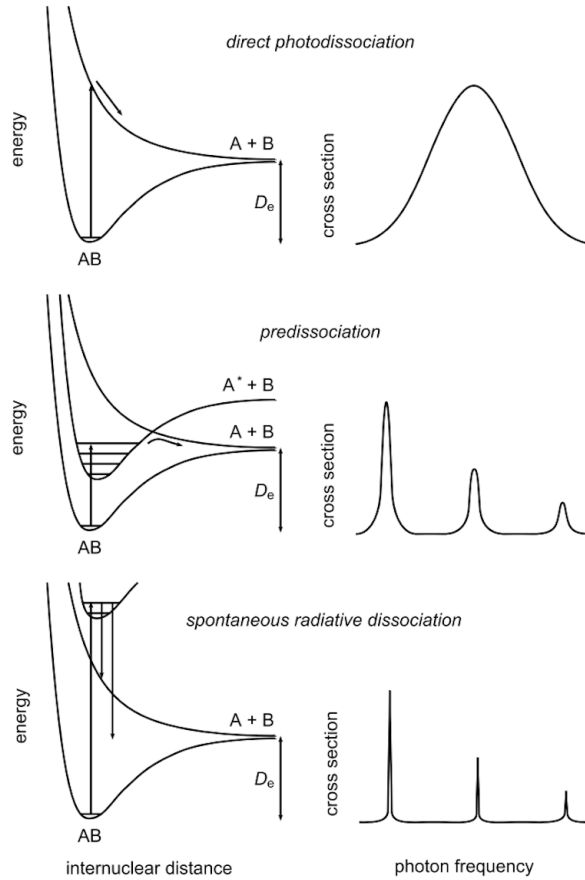
Figure 2.3: Photodissociation processes of diatomic molecules and corresponding cross sections. From top to bottom: direct photodissociation, predissociation, and spontaneous radiative dissociation from van Dishoeck & Visser (2011).

into a specific level of a bound upper state u from lower level l is

$$k_{\mathrm{pd}}^{\mathrm{line}} = \frac{\pi e^2}{mc^2} \lambda_{ul}^2 f_{ul} \eta_u x_l I(\lambda_{ul}), \tag{2.2}$$

where f_{ul} is the oscillator strength which expresses the transition probability, η_u is the dissociation efficiency of the upper level, and x_l indicates the fractional populations of the level l.

Since a molecule has many excited electronic states which can be populated by the ambient radiation field, all of the above processes will occur. A more detailed discussion can be found in van Dishoeck & Visser (2011). The main factor determining domination of line or continuous dissociation process is the structure of the molecule. For instance, photodissociation processes of H_2, CO, and N_2, which are among the most abundant molecules in

astrophysical regions, are dominated by line dissociation, while HCN is photodissociated via continuum. Photodissociation of CO and H_2 are controlled by predissociation and spontaneous radiative dissociation, respectively.

The photodissociation rate of molecules with sharp absorption bands in the UV depends on the molecular column densities. That is because all the relevant photons that can dissociate the molecules in deeper regions of the cloud can be absorbed by species near the exposed region. Thus, molecules in the deep regions are shielded from dissociation. This is called molecular shielding. As a consequence of shielding, two isotopologues of a molecule with different column densities are not equally affected by the same UV radiation field. This can lead to changes in the isotopologue ratios in UV-irradiated regions. On the contrary, isotopologues of molecules with continuum dissociation are equally affected by the radiation field. This contrast might be useful to trace the effect of UV radiation in the UV dominated regions.

Chapter 3

Observational Data

Observations of molecular emission and absorption lines in CSEs are vital in improving the current theoretical models of stellar evolution and CSE chemistry. The molecular setup in CSEs reflects the mass loss history, wind acceleration, nucleosynthesis, and dredge-up events.

In the appended papers I and II, we used new single-dish and interferometric observational data from the Atacama Pathfinder Experiment (APEX) and the Atacama Large Millimeter/submillimeter Array (ALMA) and archival data from the Swedish-ESO Submillimeter Telescope (SEST) and the Heinrich Hertz Submillimeter Telescope (HHT). In the following sections I briefly introduce facilities that are used to take new observations.

3.1 APEX

The Atacama Pathfinder Experiment (APEX) is a 12 meter antenna located at 5100 m altitude on Llano Chajnantor in Chile (Güsten et al. 2006), pictured in Fig. 3.1. In paper I, we have used two Heterodyne SIS receivers, the Swedish-ESO PI receiver for APEX (SEPIA)/band 5 (Belitsky et al. 2018a,b) and the Swedish Heterodyne Facility Instrument (SHeFI) (Belitsky et al. 2006; Vassilev et al. 2008), to observe rotational transitions of $H^{12}CN(J{=}2\text{-}1)$ and $H^{13}CN(J{=}2\text{-}1, 3\text{-}2)$ lines. The antenna main-beam efficiency, η_{mb}, the full-width half-power beam width, θ_{mb}, and the excitation energy of the upper transition level, E_{up}, and the observational frequencies are listed in Table 3.1.

In addition to our new observations, we used complementary archival data of $H^{12}CN(J{=}1\text{-}0, 3\text{-}2, \text{and } 4\text{-}3)$ and high spatial resolution ALMA observa-

Figure 3.1:   APEX telescope located at 5100 meters above sea level in the Atacama desert in northern Chile. Image credit: Maryam Saberi.

tions of H^{13}CN($J = 4 - 3$) to probe both the inner and outer CSE of R Scl.

The XS[1] and the GILDAS/CLASS[2] packages are used to reduce the single-dish observations. We subtract a first-order polynomial from the spectrum to remove the baseline. The measured antenna temperature was converted to the main-beam temperature using $T_{\rm mb} = T_{\rm A}^{\star}/\eta_{\rm mb}$.

To extend our analysis of paper I, we applied for APEX observations of H^{12}CN and H^{13}CN lines towards a sample of AGB stars with UV detections from GALEX. The aim was to analyse the rotational transitions $J =$1-0, 2-1, 3-2, and 4-3 for both HCN isotopologues for all selected sources. Therefore after an archival search, we only include the rotational transitions that have not been observed before with any other instrument. Table 3.2 lists the observed sources, their distances D, mass loss rates $\dot{M}$, and the observed transitions.

Paper II includes new CI observations with the SHeFI receiver at 492 GHz frequency. The aim of these observations was searching for CI detection towards a sample of UV bright AGB stars. The observational specifics are presented in Table 3.1.

---

[1]XS is a package developed by P. Bergman to reduce and analyse single-dish spectra. It is publicly available from ftp://yggdrasil.oso.chalmers.se

[2]http://www.iram.fr/IRAMFR/GILDAS/

Table 3.1: New observations which are included in papers I and II.

Molecule	Trans.	Freq. [GHz]	η_{mb}	θ_{mb} ["]	E_{up} [K]	Source	Instrument
$H^{13}CN$	J=2-1	172.6	0.8	35	12.4	R Scl	APEX-SEPIA
$H^{12}CN$	J=2-1	177.2	0.8	35	12.8	R Scl	APEX-SEPIA
$H^{13}CN$	J=3-2	259.0	0.75	30	24.9	R Scl	APEX-SHeFI
$H^{13}CN$	J=4-3	354.3			41.4	R Scl	ALMA-band 7
CI	$(^{3}P_1 - ^{3}P_0)$	492.2	0.6	13	23.6	omi Ceti	APEX-SHeFI
CI	$(^{3}P_1 - ^{3}P_0)$	492.2	0.6	13	23.6	V Hya	APEX-SHeFI

Table 3.2: New APEX observations of HCN isotopologues towards a sample of UV bright AGB stars.

Source	D [pc]	Mass-loss $[M_\odot \mathrm{\ yr}^{-1}]$	lines
V Hya	380	1.5×10^{-6}	$H^{12}CN$ (J=2-1,3-2, 4-3)
			$H^{13}CN$ (J=3-2, 4-3)
R Lep	130	2.0×10^{-7}	$H^{12}CN$ (J=2-1)
			$H^{13}CN$ (J=3-2,4-3)
W Hya	104	8.0×10^{-8}	$H^{12}CN$ (J=2-1)
			$H^{13}CN$ (J=3-2,4-3)
TX Psc	275	5.6×10^{-7}	$H^{12}CN$ (J=2-1,3-2,4-3)
			$H^{13}CN$ (J=3-2,4-3)
R Hya	124	3.0×10^{-7}	$H^{12}CN$ (J=2-1,3-2,4-3)
			$H^{13}CN$ (J=3-2,4-3)

3.2 ALMA

The Atacama Large Millimeter/submillimeter Array (ALMA), pictured in Fig. 3.2, is an international facility which contains 66 high-precision antennas (in Cycle 6). This includes fifty 12-m antennas in the main array which are used for sensitive and high-resolution imaging and the remaining sixteen antennas are used in the Atacama Compact Array (ACA) to enhance wide-field imaging. The ACA includes twelve 7-m antennas and four 12-m antennas for single-dish observations (Total Power Array). ALMA provides capabilities for continuum and spectral-line observations in wavelength range 0.32 mm to 3.6 mm (frequency coverage of 84 GHz to 950 GHz), and angular resolutions from 0.018″ to 3.4″ on the 12-m Array. ALMA is located on the Chajnantor plateau in Chile which provides exceptionally dry and clear sky conditions for mm/sub-mm observations.

We use the ALMA band 7 observations of $H^{13}CN$ in paper I. The high spatial resolution of the data enabled us to precisely constrain the emission

Figure 3.2: ALMA in the Atacama desert of northern Chile. Image Credit: Clem & Adri Bacri-Normier (wingsforscience.com)/ESO.

region in radial offset points from the central star which is not possible with single-dish data. The data reduction was done with the CASA.

In continuation of the work in paper II, we used ALMA band 8 to observe CI towards omi Ceti in high spatial resolution ($0.1''$-$0.3''$). Moreover, to increase the sample of CI detected AGB stars, we have performed CI observations using the ACA for a sample of eight AGB stars in Cycle 6, listed in Table 3.3.

Table 3.3: New ALMA-ACA observations of CI at 492 GHz towards a sample of UV bright AGB stars.

Source	Chemistry	D	Mass-loss
		[pc]	$[M_\odot \text{yr}^{-1}]$
W Hya	C	104	7.8×10^{-8}
R Hya	M	124	1.6×10^{-7}
U Hya	C	160	1.2×10^{-7}
EP Aqr	M	114	3.1×10^{-7}
R Leo	M	130	2.0×10^{-7}
TW Hor	C	322	2.4×10^{-8}
R Dor	M	45	6.1×10^{-7}
TX Psc	C	275	2.4×10^{-8}

Chapter 4

Radiative Transfer Modelling

All we know about stars is deduced from observations of electromagnetic radiation. Radiative transfer is the mathematical description of the transportation of radiation through a medium, in our case the CSE around an AGB star. In this chapter, I discuss the origin of molecular line emission, the theory of radiative transfer, and finally methods of solving the radiative transfer equation which are used in the appended papers.

4.1 Molecular Transitions

Molecular transitions can be divided into three categories of electronic, vibrational, and rotational transitions. Figure 4.1 shows the potential energy versus the internuclear separation for different molecular states. The most energetic molecular transitions are electronic transitions which are observable at visible or UV wavelengths. Vibrational transitions occur between different vibrational levels of the same electronic state and are mostly observable at infrared (IR) wavelengths. Stretching and bending the bonds between atoms of a molecule are the available vibrational modes and their associated energy levels strongly depend on the structure of a molecule. The least energetic transitions are rotational transitions which occur between rotational levels of the same vibrational state. Rotational transitions lie at 0.1-10 mm. Only polar molecules which possess permanent dipole moments, such as CO, can undergo the allowed rotational transitions. In order to model the observational spectra resulting from different transitions we need to calculate the probability of these transitions, which will be discussed in the following section.
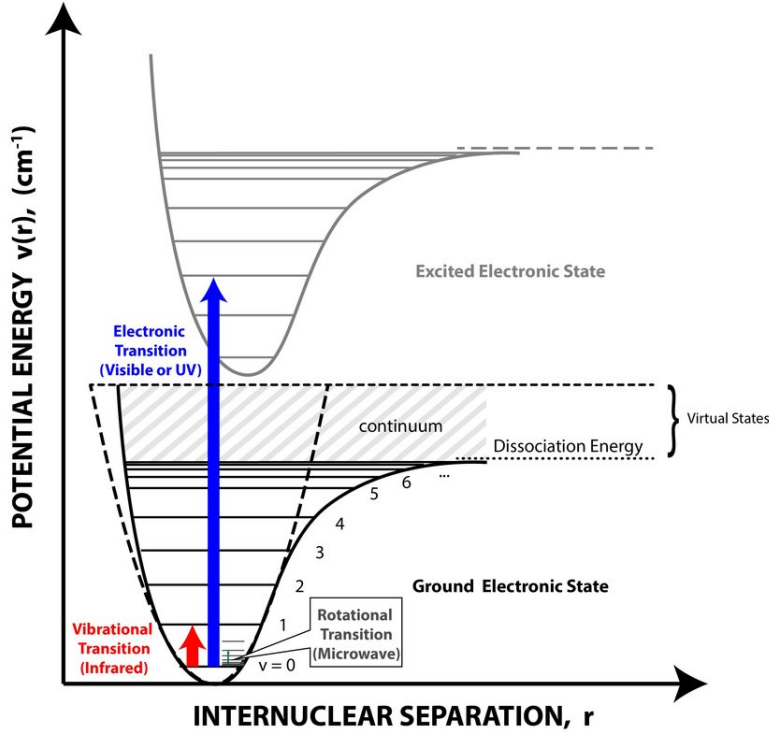
Figure 4.1: Transitions between energy levels of a molecule. Solid and dashed curves indicate potential energy associated with an anharmonic and harmonic oscillator, respectively. Image is taken from Catherine Findlay; PhD thesis, DOI: 10.5203.

4.2 Radiative Rates

There are three basic radiative processes responsible for the formation of an atomic or molecular spectral line. The three processes are referred to as spontaneous emission, stimulated emission, and absorption. The probability of each process can be expressed through Einstein coefficients.

The spontaneous emission rate per unit time for a transition from an upper state u to a lower state l with the frequency $\nu_{ul} = (E_u - E_l)/h$ can be expressed by the corresponding Einstein A_{ul} coefficient

$$A_{ul} = \frac{8\pi^2\nu^3}{3\epsilon_0\hbar c^3}|\mu_{ul}|^2 \quad s^{-1}, \tag{4.1}$$

where μ_{ul} is the transition dipole moment, ϵ_0 is the vacuum permittivity, c is the speed of light in vacuum, and $\hbar = h/2\pi$ where h is Planck's constant. The spontaneous transition releases a photon with the energy $h\nu = E_u - E_l$.

The rate of stimulated emission is expressed by the Einstein B_{ul} coefficient

as

$$B_{ul} = \frac{|\mu_{ul}|^2}{6\epsilon_0 \hbar}. \tag{4.2}$$

The two rates of spontaneous and stimulated emission are related via:

$$A_{ul} = \frac{8\pi h \nu^3}{c^3} B_{ul}. \tag{4.3}$$

And finally the rate of absorption B_{lu} can be written in terms of the stimulated emission rate

$$B_{lu} g_l = B_{ul} g_u, \tag{4.4}$$

where g is the statistical weight of the level.

We should note that spontaneous emission does not depend on the radiation field. However, the stimulated emission and absorption processes depend on the radiation field and their probability are linearly proportional to the spectral energy density of the radiation field.

4.3   Collisional Rates

In addition to the interaction between molecules and electromagnetic radiation, a molecular transition between energy levels can also occur through collision of a molecule with other abundant species such as H_2 and He. In the CSEs of AGB stars, H_2 is the most abundant molecule and because of that we consider its collisional rate with the molecule of interest in the modelling.

The collisional de-excitation rates are given by

$$C_{ul} = n_{\text{col}} c_{ul}, \tag{4.5}$$

where n_{col} is the number density of collisional partner and c_{ul} is the collisional de-excitation coefficients in cm^3s^{-1}.

The collisional excitation rates can be related to de-excitation rates by

$$C_{lu} = C_{ul} \frac{g_u}{g_l} e^{-(E_u - E_l)/kT_{\text{kin}}}, \tag{4.6}$$

where k is the Boltzman constant and T_{kin} is the gas kinetic temperature.

The Einstein A coefficients of a molecule of interest and its collisional rates with H_2 are input to the radiative transfer code.

4.4   Radiative Transfer Equations

The specific intensity I_ν is defined as the energy per unit time, frequency, solid angle, and area and has units erg cm^{-2} s^{-1} Hz^{-1} ster^{-1}. The specific intensity is constant while the ray passes through vacuum. However, propagation of radiation through matter causes changes in the specific intensity due to emission, absorption, and scattering (Fig. 4.2). In the absence of scattering, the changes in a beam after passing a distance ds through matter is given by

$$dI_\nu = j_\nu ds - \kappa_\nu I_\nu ds, \tag{4.7}$$

where j_ν is the emission coefficient and κ_ν is the absorption coefficient at frequency ν. In this equation, the first term describes the intensity added to the beam, and the second term describes the intensity subtracted after passing a distance ds. The ratio of the j_ν and κ_ν is defined as the source function:

$$S_\nu \equiv \frac{j_\nu}{\kappa_\nu}, \tag{4.8}$$

which has the same units as the specific intensity. The source function for a transition between states u and l can be expressed using the Einstein coefficients as

$$S_{ul} = \frac{n_u A_{ul}}{n_l B_{lu} - n_u B_{ul}}. \tag{4.9}$$

The absorption coefficient integrated over path-length through the atmosphere gives a quantity called the optical depth as follow

$$d\tau_\nu \equiv \int \kappa_\nu ds, \tag{4.10}$$

which is dimensionless and indeed counts the number of photon mean free paths along the direction ds. If we replace the geometrical depth ds with an optical depth $d\tau$ defined above, the radiative transfer equation 4.7 can be written as

$$\frac{dI_\nu}{d\tau_\nu} = S_\nu - I_\nu, \tag{4.11}$$

The solution for the simplified transfer equation 4.11 can be written

$$I_\nu = I_\nu(0)e^{-\tau} + \int_0^{\tau_\nu} S_\nu(\tau_\nu')e^{-(\tau_\nu - \tau_\nu')}d\tau_\nu', \tag{4.12}$$
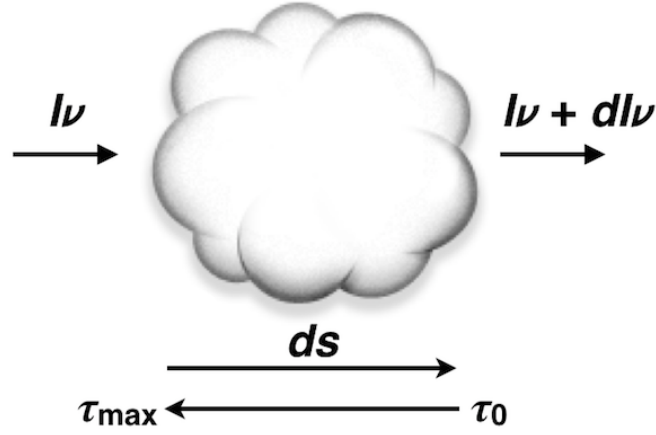
Figure 4.2: Illustration of the propagation of radiation through a cloud with a geometrical depth *ds* and an optical depth τ.

the first term represents the amount of radiation absorbed from the background intensity $I_\nu(0)$ and the second term accounts for the radiation emitted and re-absorbed within the medium.

In order to solve the radiative transfer equation, the molecular level populations are required. In calculating the molecular level populations, we consider that there is a balance between all the upward and downward processes which populate and de-populate each state of a molecule. This is called statistical equilibrium (SE). In SE, all the rate equations can be written as

$$\frac{dn_i}{dt} = 0. \tag{4.13}$$

Thus, the statistical equilibrium system of equations can be written:

$$\sum_{l<u}[n_u A_{ul} - (n_l B_{lu} - n_u B_{ul})\bar{J}_{ul}] - \sum_{l>u}[n_l A_{lu} - (n_u B_{ul} - n_l B_{lu})\bar{J}_{ul}]$$
$$+ \sum_{u,l}(n_u C_{ul} - n_l C_{lu}) = 0, \tag{4.14}$$

where $\bar{J}$ is the mean intensity obtained by integrating the specific intensity over solid angle Ω and averaged over all directions μ and can be written as:

$$\bar{J} = \frac{1}{4\pi} \int d\Omega \int d\nu \varphi_\nu(\mu) I_\nu(\mu), \tag{4.15}$$

where I_ν is the specific intensity along direction μ with frequency ν and $\varphi_\nu(\mu)$ is a weight function.

Both radiative transfer codes, ALI and MCP, that we use in the appended papers solve equations 4.12 and 4.14 using iterative methods. Further discussions are presented in Sect. 4.7 and 4.8.

4.5   CSE Properties

In our radiative transfer calculations we assume a spherically symmetric CSE created by a constant mass-loss rate. The CSE is smoothly accelerating. Three radiation fields are considered to affect molecular excitation in the CSE: the stellar radiation field, the dust radiation field, and the cosmic microwave background (CMB) radiation field. In calculating the stellar radiation field we assume that the star is a blackbody of temperature T_{eff}, the effective stellar temperature, which is derived through modelling of the spectral energy distribution (SED). The dust radiation field is defined by the dust temperature profile and the dust density distribution. The CMB radiation field is calculated by assuming a blackbody with a constant temperature of 2.7 K. Other CSE parameters such as the gas temperature profile, the expansion velocity and molecular distributions profiles are discussed in detail in the appended papers.

4.6   Dust Properties

To model the radiative contribution from the dust in the CSE, we set the dust optical depth τ at a reference wavelength $\lambda = 10\mu m$. The optical depth τ should come out of a spectral energy distribution (SED) model. We use two dust opacity profiles for silicate and carbon dust which are shown in Fig. 4.3. The dust grain radius is assumed to be 0.1 μm with densities $\rho_d = 3.5$ g cm^{-3} for both carbon and silicate dust. The gas-to-dust mass ratio is assumed to be 200 for all models.

4.7   The Accelerated Lambda Iteration Method

One of the most commonly used methods of solving the radiative transfer equation is the Accelerated Lambda Iteration (ALI) method. The ALI method is described in detail by e.g. Scharmer (1981) and Rybicki & Hummer (1991). The code used in paper I is based on the ALI method and has been implemented by Per Bergman. The code has been described and tested
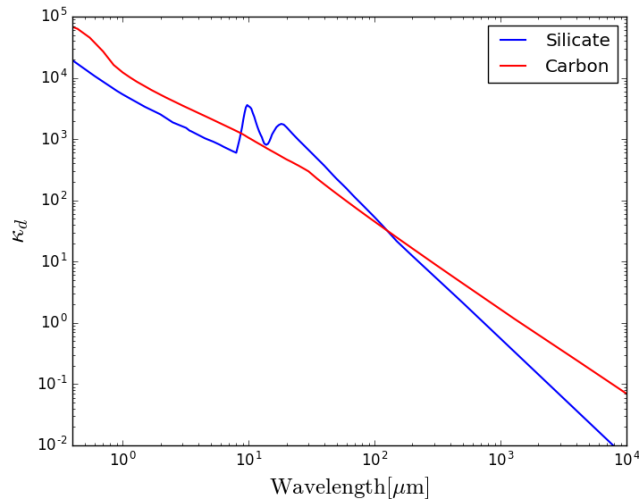
Figure 4.3: The dust opacity dependence on wavelength for silicate and carbon dust.

in e.g. Maercker et al. (2008, 2009). In the ALI method, $I_{\mu\nu}$ is derived by using an operator Λ which acts on the source function S and gives the specific intensity at any radial point as

$$I_\nu(\mu) = \Lambda_{\mu\nu} S_{\nu,\text{tot}}(\mu) + I_{\text{bg}}, \tag{4.16}$$

where the source function $S_{\nu,\text{tot}}(\mu)$ includes all contributions from dust and overlapping lines and I_{bg} is contribution from the background. The Λ operator is an $N \times N$ dimensional matrix where N is the number of radial points. The diagonal elements describe the local contribution and the off-diagonal elements the contribution from other parts of the emitting region.

The code starts with an initial guess for the level populations to solve the SE equation (Eq. 4.14). Then, the specific intensity is calculated at any radial point. The derived populations from the last iteration will be used to solve a new SE equation. This process is continued until convergence of the level populations is obtained. In the ALI method, the high optical depths are computed separately which makes the code converge quickly at high optical depths and that is where the "accelerated" part of the ALI comes from.

4.8 The Monte-Carlo Program

The Monte-Carlo program (MCP) code that we have used is previously discussed in Schöier & Olofsson (2001); Schöier et al. (2002); Ramstedt et al. (2008). The CSE is divided into a number of concentric shells which are irradiated by model photons. Each model photon corresponds to a large number

of real photons. As model photons pass through each shell their weight will be changed due to absorptions and emissions. The code calculates the number of excitations and de-excitations the model photon causes on its way through the cloud in each region. This will be used as an estimate of the mean integrated intensity. In the MCP, to lower the random errors we need to increase the number of stimulated photons which require large computing time. Therefore, the MCP may not be very efficient at modelling high optical depths.

One of the main difference between our ALI and MCP codes is that the MCP includes the energy balance equation while ALI does not. Therefore, MCP is usually used for excitation analysis of CO because it is able to take heating and cooling into account and ALI is used for other molecules especially when optical depth effects cause MCP to take a particularly long time to reach convergence.

Chapter 5

Chemical Modelling

To simulate the chemistry of a CSE surrounding an evolved star we use an extended version of the publicly available code rate13-cse[1]. A detailed discussion on the code can be found in McElroy et al. (2013) and references therein. In this Chapter I briefly introduce the original code and explain new additions and modifications to it.

5.1 CSE Properties

The code assumes a spherically symmetric CSE which is formed due to a constant mass loss from an evolved star. It is expanding with a constant velocity V_{exp}. The mass loss rate $\dot{M}$ and the expansion velocity V_{exp} are two free parameters which determine the H_2 number density distribution throughout the envelope $n_{H_2}(\mathrm{r})$ which falls as $1/r^2$ (r is the distance from the central star). The envelope is exposed to the isotropic standard interstellar radiation field (ISRF) derived by Draine (1978). The Draine ISRF intensity is expressed as

$$I_{\mathrm{ISRF}}(\lambda) = \left(\frac{6.36 \times 10^7}{\lambda^4} - \frac{1.0237 \times 10^{11}}{\lambda^5} + \frac{4.0812 \times 10^{13}}{\lambda^6} \right), \qquad (5.1)$$

where I is in unit ergs cm$^{-2}s^{-1}$Å^{-1} and λ is in Å.

---

[1]http://udfa.ajmarkwick.net

The gas kinetic temperature profile of a CSE can be approximated by a power-law function as

$$T_{\text{kin}}(r) = T_{\text{i}}(\frac{r_{\text{i}}}{r})^{\beta},$$

(5.2)

where β is typically assumed to be $\beta = 0.4 - 1.0$ and determines the slope of the profile, and T_{i} is the temperature at the inner radius r_{i} (e.g. De Beck et al. 2012; Danilovich et al. 2014; Khouri et al. 2014; Maercker et al. 2016; Ramos-Medina et al. 2018). The minimum temperature at the outer edge of CSE is assumed to be 10 K.

5.2 Dust

The code assumes that the dust absorption is independent of the wavelength. We also ignore dust scattering and assume that the dust absorption dominates the dust extinction. Therefore, we consider a constant dust extinction at 1000 Å, as Morris & Jura (1983), to be:

$$\tau_{\text{dust}}(r, 1000\text{Å}) = \frac{4.65 \times 2 \times N_{\text{H}_2}(r)}{1.87 \times 10^{21}},$$

(5.3)

where N_{H_2} is the H$_2$ column density to infinity. We assume the gas/dust = 200, grain radius 0.1 μm, and dust grain density $\rho = 3.5$ g cm^{-3} for all models.

5.3 The Chemical Network

We have used the upgraded version of the UMIST Database for Astrochemistry (UDfA) which contains ^{13}C and ^{18}O isotopes, all corresponding isotopologues, their chemical reactions and the properly scaled reaction rate coefficients (Röllig & Ossenkopf 2013). The chemical network includes 934 species (351 neutral species, 572 cations, and 11 anions) and 15108 gas-phase reactions to describe the chemistry of the CSEs. The chemical network contains two-body reactions, photo-processes, and cosmic-ray processes. Table 5.1 lists all the reaction types that are included in the chemical network.

Two-Body Reactions

A two-body reaction can be simply expressed as

$$A + B \ \rightarrow \ C,$$

(5.4)

where the reactants A and B can be atoms, molecules, ions, or electrons. The rate of C abundance enhancement with time per unit volume is expressed by $n(C)$ and can be derived as

$$\frac{dn(C)}{dt} = k\, n(A)\, n(B) \quad [\text{cm}^{-3}\text{s}^{-1}], \tag{5.5}$$

where k is the reaction rate that can be calculated using the Arrhenius-type formula:

$$k = \alpha \left(\frac{T}{300}\right)^{\beta} \exp\left(\frac{-\gamma}{T}\right) \quad [\text{cm}^3\text{s}^{-1}], \tag{5.6}$$

where T is the gas temperature, α [cm^{3}s^{-1}] is a pre-exponential factor, β indicates the temperature dependence of the rate coefficient, and γ [K] is the activation energy or energy barrier of the reaction. Two-body reactions can be divided into several types which are given in Table 5.1.

Photo-Processes

The photo-processes can be divided into photo-dissociation and photo-ionization processes. The reaction rate of photo-reactions is calculated as

$$k = \alpha \exp(-\gamma A_v) \quad [\text{s}^{-1}], \tag{5.7}$$

where α [s^{-1}] is the photodissociation rate in the unshielded region, A_v [mag] is the extinction by the dust in the visible wavelength range and γ is a parameter that takes into account the increased extinction at ultra-violet wavelengths compared to the visible. For the CO molecule, the photodissociation rate is calculated in more detail in Sect. 5.5.1.

Cosmic-Ray Processes

There are two types of cosmic-ray reactions. Direct cosmic-ray ionization reactions for which the reaction rate is simply

$$k = \alpha \quad [\text{s}^{-1}], \tag{5.8}$$

and cosmic-ray induced photo-reactions for which the reaction rate is calculated according to

$$k = \alpha \left(\frac{T}{300}\right)^{\beta} \frac{\gamma}{1-\omega} \quad [\text{s}^{-1}], \tag{5.9}$$

where α [s^{-1}] is the cosmic-ray ionization rate, γ is the efficiency of the cosmic-ray ionization, ω ($0 \leqslant \omega \leqslant 1$) is the dust-grain albedo in the far-UV, and T is the gas temperature.

Table 5.1: All reaction types that are included in the chemical network of the CSE code.

Code	Reaction Type	Example	Num[1].
	Tow-Body Reactions		
IN	Ion-Neutral	$A^+ + BC \rightarrow AC^+ + B$	8737
NN	Neutral-Neutral	$A + BC \rightarrow B + AC$	1986
CE	Charge Exchange	$A^+ + BC \rightarrow BC^+ + A$	1536
DR	Dissociative Recombination	$AB^+ + e^- \rightarrow A + B$	1273
RA	Radiative Association	$A + B \rightarrow AB + h\nu$	294
AD	Associative Detachment	$A + B \rightarrow AB^+ + e^-$	136
CD	Collisional Dissociation	$A + BC \rightarrow A + B + C$	44
MN	Mutual Neutralisation	$A^- + BC^+ \rightarrow A + BC$	39
RR	Radiative Recombination	$A^+ + e^- \rightarrow A + h\nu$	28
REA	Radiative Electron Attachment	$A + e^- \rightarrow A^- + h\nu$	8
	Photo-Processess		
PH	Photo Process (Dissociation)	$AB + h\nu \rightarrow A + B$	568[2]
PH	Photo Process (Ionization)	$AB + h\nu \rightarrow AB^+ + e^-$	
	Cosmic-Ray Processess		
CR	Cosmic-Ray Photon (CRPHOT)	$A + \mathrm{CRPHOT} \rightarrow B + C$	443
CP	Cosmic-Ray Proton (CRP)	$A + \mathrm{CRP} \rightarrow A^+ + e^-$	16

NOTE: 1. Number of reactions in the chemical network. 2. This is the total number of photo-processes.

5.4   Molecular Abundance Distributions

Assuming that the mass-loss rate $\dot{M}$ and the CSE expansion velocity V_{exp} are constant in time, the abundances of different circumstellar species relative to H$_2$ number density, $f_i(r) = n_i(r)/n_{\mathrm{H2}}(r)$, are calculated at each radial point by solving an ordinary differential equation as follows

$$\frac{df_i}{dr} = \frac{1}{v_e}\left[\sum_{j,k} k_{jk} f_j f_k n(r) + \sum_l k_l f_l - f_i\left[\sum_m k_{im} f_m n(r) + \sum_n k_n\right]\right], \quad (5.10)$$

where the two first terms count all the reactions which lead to creation of the species i by two-body reactions and photo-processes and/or cosmic-ray processes. The two last terms count all the reactions which lead to destruction of the species i through reactions with species m or through CR or photoprocesses. The rate coefficient for each reaction is given by k.

5.5 The CO Envelope Size

I discuss here the two processes that predominantly determine the abundance distributions of ^{12}CO and ^{13}CO in the outer CSE: dissociation of CO by interstellar photons and chemical fractionation, a process which leads to isotope exchange between species.

5.5.1 Photodissociation of CO

The CO molecule photodissociates by absorbing photons at specific frequencies in the wavelength range 911.75 - 1117.8 Å (e.g. Visser et al. 2009). Therefore, it is subject to self-shielding by CO molecules closer to the UV source and mutual-shielding by other abundant species such as H_2, H, C and dust particles which are dissociated at the same wavelengths. The amount of shielding depends on the UV intensity, the gas temperature, and the column density of CO and other shielding species. Since ^{12}CO is more abundant than all other CO isotopologues, it is subject to more shielding than the less abundant isotopologues. This can lead to variations in the ^{12}CO/^{13}CO isotopologue abundance ratio throughout the CSE.

In the original rate13-cse code, it is simply assumed that CO photodissociates by absorbing photons only in one band at 1000 Å and the CO shielding is calculated using a single-band approximation (Morris & Jura 1983). However, the latest laboratory measurements have shown that CO has 855 dissociating lines in the UV arising in rotational levels $J = 0$ to 9 in the lowest vibrational state $v = 0$. We have modified the CO photodissociation treatment of the code considering all dissociating lines to more precisely derive the CO photodissociation radius. Here, I summarize the calculations of the CO photodissociation rate. Detailed discussions are presented in the third paper.

The total CO photodissociation rate at radius r is the summation of the photodissociation rates of all discrete contributing lines i as following:

$$k(r) = \sum_{i=1}^{855} k_i^0 \, \beta_i(r) \, \gamma_i(r) \quad [s^{-1}], \tag{5.11}$$

where k_i^0 is the CO unshielded photodissociation rate at the edge of the CSE, β_i is the CO self-shielding efficiency and γ_i accounts for the shielding by species other than CO. The k_i^0 can be calculated using:

$$k_i^0 = \frac{\pi e^2}{m_e c^2} \, f_i \, \eta_i \, x_l \, \lambda_i^2 \, I_{\text{ISRF}}(\lambda_i) \quad [s^{-1}], \tag{5.12}$$

where f is the absorption oscillator strength that expresses the probability of absorption of electromagnetic radiation in transitions between energy levels of a molecule, η is the probability for dissociation of the upper level, x_l is the fractional populations of the lower level and I_{ISRF} is the mean intensity of the interstellar radiation field in unit photons cm^{-2} s^{-1} Å^{-1}. The constant factor $\pi e^2/m_e c^2$ takes the value 8.85×10^{-21} if λ is in Å. From this calculation, k_i^0 is estimated to be 2.6×10^{-10} s^{-1}.

We use the approximations by Morris & Jura (1983) for the CO shielding by itself (β) and by H$_2$ and dust (γ) given as

$$\beta_i(r) = \frac{1 - \exp(-1.5\,\tau_{CO}(\nu_i, r))}{1.5\,\tau_{CO}(\nu_i, r)}, \tag{5.13}$$

where $\tau_{CO}(\nu_i, r)$ indicates the CO optical depth of each dissociating line i at radius r and

$$\gamma_i(r) = \exp\left(-\alpha\left(\tau_{\text{dust}}(r) + \tau_{\text{H}_2}(\nu_i, r)\right)^b\right), \tag{5.14}$$

where $\alpha = 1.644$ and $b = 0.86$. τ_{H_2} is the H$_2$ opacity at each CO dissociating line i.

Figure 5.1 presents the impact of each shielding species on the CO abundance distribution in a CSE of an AGB star with a mass-loss rate $\dot{M} = 10^{-5}\ M_\odot\text{yr}^{-1}$, an expansion velocity $V_{\text{exp}} = 15$ km s^{-1}, and the initial CO fractional abundance $f_{\text{CO/H}_2} = 8 \times 10^{-4}$.

We have implemented the shielding functions only for the ^{12}C^{16}O and ^{13}C^{16}O isotopologues. We have found that considering the shielding functions for the ^{13}C^{18}O and ^{12}C^{18}O isotopologue does not change their distributions. Thus, we deactivate their shielding function calculations to decrease the computation time.

The CO abundance distribution can be represented with an analytical formula derived by Mamon et al. (1988):

$$f_{\text{CO}} = f_0 \exp\left(-ln(2)\,(\frac{r}{r_{1/2}})^\alpha\right), \tag{5.15}$$

where f_0 is the initial CO/H$_2$ abundance close to the star, α determines the steepness of the profile, and $r_{1/2}$ marks the radius where the CO abundance drops to half of its initial value. We have derived $r_{1/2}$ and α for a large grid of models consisting of 10 values for f_0 ($1, 2, \cdots, 10 \times 10^{-4}$), 13 values for $\dot{M}$ ($[1, 2, 5] \times 10^{-8}, [1, 2, 5] \times 10^{-7}, \cdots, 1 \times 10^{-4}\ M_\odot$ yr^{-1}), and 3 values for V_{exp} (7.5, 15, 30 km s^{-1}). Our results show that the CO envelope size should be smaller than the commonly used radii in the literature. The discrepancy
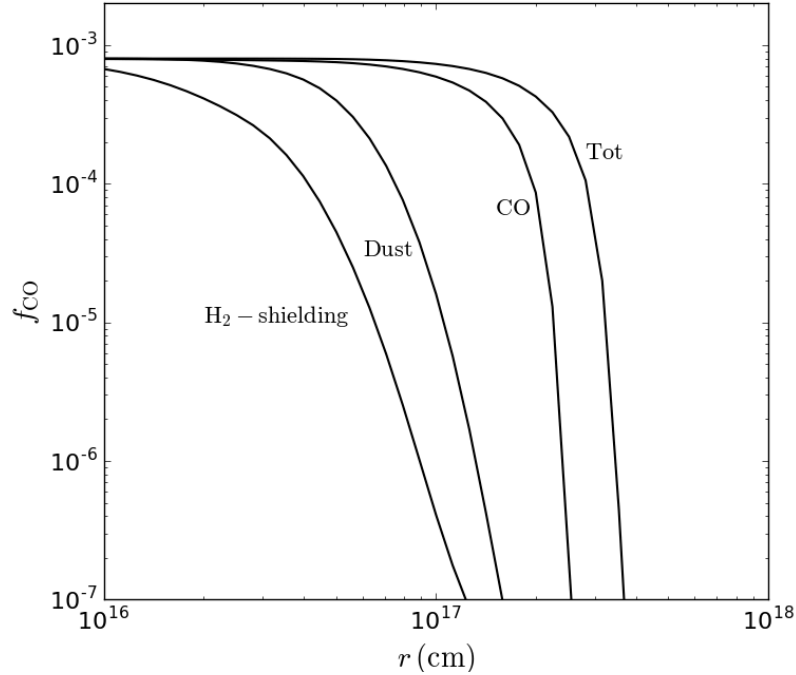
Figure 5.1: The CO fractional abundance distributions for simulations with different shielding functions that regulate CO photodissociation: shielding by H_2, shielding by dust, CO self-shielding, and the total shielding for a model with mass-loss rate $\dot{M} = 10^{-5} M_\odot \text{ yr}^{-1}$, an expansion velocity $V_{\text{exp}} = 15 \text{ km s}^{-1}$, and the initial CO/H_2 fractional abundance $f_{CO} = 8 \times 10^{-4}$.

depends on both the CSE parameters and the intensity of the ISRF. We have also examined the effect of varying five fundamental parameters: the CO excitation temperature T_{ex}, the mass-loss rate $\dot{M}$, the expansion velocity of the CSE V_{exp}, the initial CO abundance f_0, and the strength of the ISRF on the CO envelope size. The results are discussed in detail in paper III.

5.5.2   The CO Fractionation Reaction

The CO fractionation reaction is given by Watson et al. (1976)

$$^{13}C^+ +^{12}CO \; \rightleftharpoons \; ^{12}C^+ +^{13}CO + \Delta E, \qquad (5.16)$$

where $\Delta E = 35$ K. At high temperatures the forward and backward reaction rates are equal, however at low temperatures ($T < 100$ K) the backward reaction rate gets lower resulting in a one-way channel which favors creation of ^{13}CO from ^{12}CO. Therefore, at low temperatures, this leads to a change in the $^{12}CO/^{13}CO$ ratio. In the outer CSE where the temperature is low ($T <$
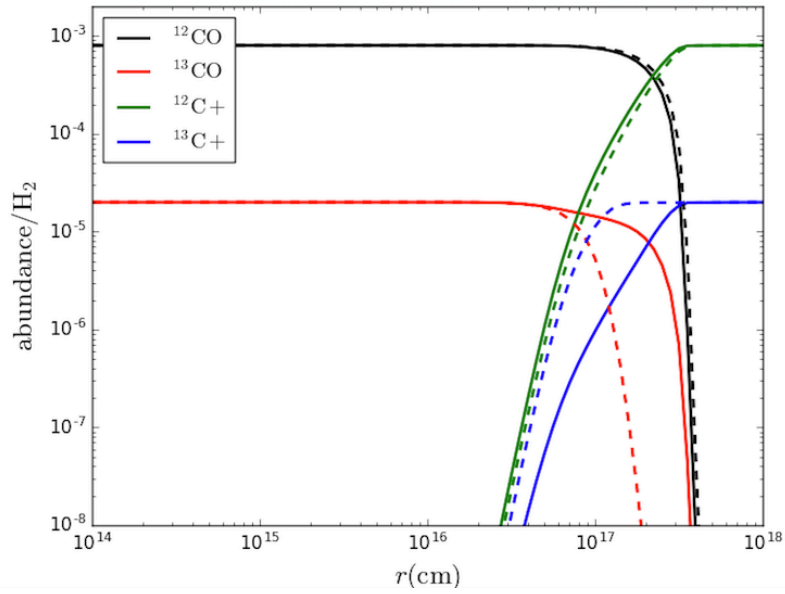
Figure 5.2:   The CO and C$^+$ abundance distributions with (solid line) and without (dashed line) considering the CO fractionation reaction in the chemical network.

100K), the fractionation reaction can substantially change the ^{12}CO/^{13}CO abundance ratio as shown in Fig. 5.2.

Chapter 6

Introduction to appended papers

In this chapter I describe the motivation and goals of the studies presented in the four appended papers. I also summarize the results of our detailed analysis and give an outline of the ongoing and future plans to follow up the work presented in each paper.

6.1 Paper I

The photospheric ^{12}C/^{13}C ratio is a good tracer of the stellar nucleosynthesis. From an observational point of view, a direct estimate of the ^{12}C/^{13}C ratio is very challenging. Hence, observing isotopologues of circumstellar carbon-bearing molecules are widely used to trace the elemental isotopic carbon ratio. It is generally assumed that the circumstellar isotopologue ratios are representative of the stellar isotopic ratios (e.g. Schöier & Olofsson 2000; Milam et al. 2009; Ramstedt & Olofsson 2014). However, spatially resolved ALMA observations of the CSE of a carbon-type AGB star R Scl show that there is a variation in the ^{12}CO/^{13}CO ration in different parts of the CSE associated with different mass-loss epochs. Vlemmings et al. (2013) find an average value of ^{12}CO/^{13}CO ~ 19 in the detached shell, consistent with the atomic carbon photospheric ratio of ^{12}C/^{13}C $\sim 19 \pm 6$ reported by Lambert et al. (1986), whereas they derive a lower limit of ^{12}CO/^{13}CO > 60 for the present-day mass loss. Vlemmings et al. (2013) suggested that the lack of ^{13}CO in the recent mass loss might be due to extra photodissociation of ^{13}CO by internal UV radiation from a previously unknown binary companion and/or stellar chromospheric activity, while the more abundant ^{12}CO would be self-shielded. This hypothesis can be examined by measuring the isotopologue ratio of a circumstellar molecule which dissociates through

continuum (e.g. HCN) and is therefore not subject to self-shielding. For molecules with continuum photodissociation we do not expect any variation in the isotopologue ratio caused by photodissociation.

In paper I we performed a detailed radiative transfer analysis of $H^{12}CN$ and $H^{13}CN$. Our analysis shows that the $H^{12}CN/H^{13}CN = 26.3 \pm 11.9$ ratio in the inner CSE is consistent with the photospheric $^{12}C/^{13}C = 19 \pm 6$ ratio. These results support the idea that the CO isotopologue selective photodissociation by the extra UV-radiation could be the main reason of the observed discrepancy between CO isotopologue and C isotope ratios in R Scl, as suggested by Vlemmings et al. (2013). Our results suggest that the circumstellar HCN isotopologue ratio might be a more reliable tracer of the photospheric C isotopic ratio in UV dominated envelopes.

6.1.1 Follow-up work

Further investigations are needed to prove whether the $H^{12}CN/H^{13}CN$ ratio is a better tracer of the $^{12}C/^{13}C$ compared to the widely used $^{12}CO/^{13}CO$ ratio in the UV dominated regions. Therefore, I have applied for $H^{12}CN$ and $H^{13}CN$ observations with the APEX telescope for another nine UV bright AGB stars. These were granted and partly carried out in August 2017. The list of observed sources and lines is presented in Table 3.2. For all the selected sources there is archival CO data. Our aim with these observations is to compare the circumstellar CO and HCN isotopologue ratios with the atomic C isotopic ratio for a larger sample of UV active AGB stars.

Moreover, the work presented in paper IV is a continuation of this project to investigate variations of both CO and HCN isotopologue ratio in the outflow of AGB stars under different conditions.

6.2 Paper II

UV radiation plays a critical role in the chemistry of CSEs around evolved stars through UV photodissociation and photoionization. Destruction of C-bearing molecules by either UV photo-dissociation or shock-dissociation is expected to generate a considerable amount of atomic carbon in the CSE (e.g. Glassgold & Huggins 1986; Cherchneff & Glassgold 1993; Knapp et al. 2000). An enhancement of the CI line emission from these environments can, therefore, probe UV- and shock-induced chemistry.

Accordingly, I applied for CI observations towards nine UV bright AGB stars using APEX. These were granted and partly performed in August 2017.

Two sources out of nine, omi Ceti and V Hya, have been observed and we find CI line emissions in both cases.

Paper II presents the CI observational results for omi Ceti and V Hya. In case of omi Ceti, it is the first time that CI line emission is detected towards an oxygen-rich AGB star. Our detection of CI towards V Hya confirms its previously tentative CI detection reported by Knapp et al. (2000).

The results of the omi Ceti observations were surprising since we found a shift (~ 4 km s^{-1}) between the omi Ceti stellar velocity and the peak of the CI line emission. omi Ceti belongs to a symbiotic binary system, the Mira AB system, with a separation $\sim 0.5''$ between two stars. To explain the velocity shift, we suggested that CI arises from a compact region near the binary companion due to the strong UV emission originating from the accretion process. The velocity shift could then be the result of the orbital velocity of the companion.

6.2.1 Follow-up work

To confirm our suggested hypothesis for explaining the observed velocity shift of CI towards omi Ceti we required high-spatial resolution observations which could more precisely locate the emission region. Therefore I have applied for high-spatial resolution (0.1$''$-0.3$''$) ALMA band-8 observations of CI in Cycle 6. These were granted and carried out in Dec 2018. Figure 6.1 presents our recent ALMA main-array CI observations and the CI data from APEX. The ALMA observations show a tentative double-peaked spectrum. Since we do no detect compact emission and only recover $< 10\%$ of the emission seen with the APEX, we can conclude that the emission is spread over 2.5$''$ ($\sim 3 \times 10^{15}$ cm) and we thus rule out the hypothesis from paper II. The velocity shift is therefore likely due to the known complicated structure of the Mira A wind shaped by the Mira B interaction (Ramstedt et al. 2014).

To extend our sample of CI detections towards AGB stars, I have applied for ACA observations in Cycles 6 and 7 towards another eight nearby UV bright AGB stars listed in Table 3.3. All Cycle 6 targets were observed. We include Mira in the ACA observations in Cycle 7 to recover as much as possible of the flux lost with the 12-m observations and map the structure of CI in its envelope. Our Cycle 7 proposal is also accepted.

Moreover, to estimate the C budget and make a more complete picture of the CO photodissociation mechanism in CSEs of our sample of AGB stars, I also applied for CII observations with the SOFIA telescope. These were unfortunately not approved in Cycle 7. We plan to reapply for Cycle 8. The combined ACA and SOFIA data will enable us to have a full picture of the
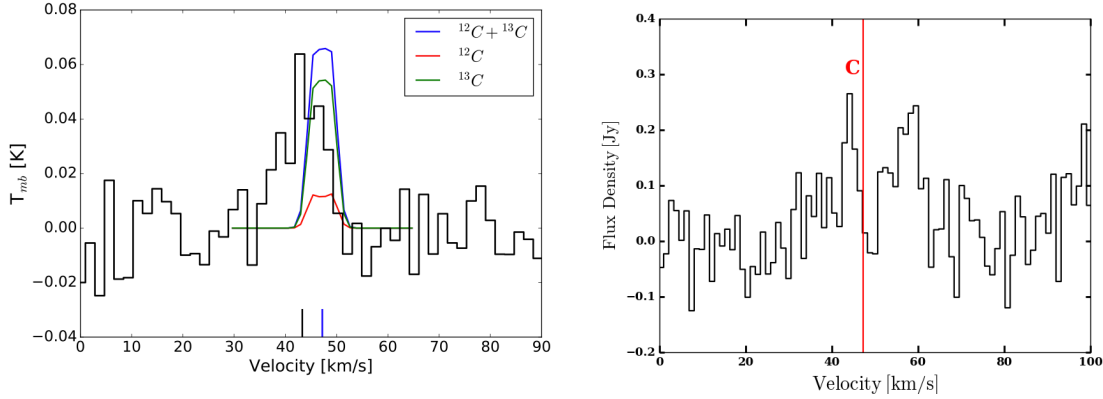
Figure 6.1: **Left panel:** $C(^3P_0 - ^3P_1)$ spectrum (black) of omi Ceti from single dish APEX telescope with a beam of $11.8''$ taken at the stellar position (Saberi et al. 2018). The stellar $V_{LSR} = 47.2$ km/s and the observations peak $V_{LSR} = 43.4$ km/s are indicated as vertical markers on the x-axis in blue and black, respectively. The results of the radiative transfer modelling of ^{12}C and ^{13}C are shown in red and green, respectively. The blue profile indicates the total amount of C. **Right panel:** ALMA main-array observations of CI emission towards omi Ceti. This is extracted with a beam of $2.5''$. The red line corresponds to the carbon frequency at the V_{LSR} of omi Ceti.

carbon budget, and hence put more constraints on the CO dissociation and ionization mechanisms.

6.3   Paper III

CO is the second most abundant molecule after H_2 in CSEs around evolved stars. Since CO is easily observable and chemically stable, it has been extensively used to constrain CSE properties such as mass-loss rate, gas expansion velocity, and gas temperature profile. Therefore an accurate determination of the CO abundance is crucial in understanding CSE properties. A key process in controlling the abundance and distribution of CO throughout a CSE is photodissociation by UV photons. CO photodissociation occurs through specific lines in the UV region. This process makes CO strongly subject to shielding by species which are dissociated at the same wavelengths. The amount of shielding depends on the column density of shielding species, as well as on the physical properties of the astrophysical region such as the geometry and temperature and the intensity of the UV radiation field. All these parameters should be carefully taken into account in the calculation of the CO envelope size around AGB stars.

In paper III, we have updated calculations of the depth dependency of the CO photodissociation rate for an expanding CSE using the latest laboratory measurements. We examine the effects of varying five primary parameters on

the CO abundance distribution: mass-loss rate, expansion velocity, initial CO abundance, CO excitation temperature, and intensity of the ISRF. In general our results predict smaller CO envelope sizes compared to the most commonly used radii in the literature. We have shown a strong sensitivity of the CO distribution with the AGB chemical type (due to the varying CO abundance) that has not been considered in modelling before. We also demonstrate that modest variations of the ISRF can significantly impact the CO distributions, whereas it is generally assumed that CSEs are irradiated by a standard ISRF such as those presented by Draine (1978) and Jura (1974) which are measured in the solar neighborhood. There is clear evidence that the ISRF is different for stars located in clusters or which lie above the galactic plane. This can significantly affect the CO distribution estimates and therefore mass-loss rate estimates.

6.3.1 Follow-up work

High-resolution ALMA observations, e.g. those from the DEATHSTAR project (Ramstedt et al. in prep), can together with our new formalism of determination of the CO envelope size, be used to decrease the uncertainty in mass-loss rate determinations.

In paper III we assumed that the CSE is irradiated by only the ISRF. However, as mentioned before, we are aware of the presence of internal sources of UV radiation for a large sample of AGB stars. We do not expect the internal sources of UV radiation to significantly alter the CO envelope size. However we do expect that it impacts the chemistry of the inner region. To simulate the effect of an internal source of UV radiation we implement an internal source of UV radiation in our CSE-chemistry code. Figure 6.2 shows preliminary results of adding a blackbody with T = 18000 K in the chemical code. As can be seen, there is an enhancement of CI and CII in the inner CSE. A further detailed analysis of the consequences of the presence of an internal UV radiation, both blackbody and real UV spectra from GALEX, on the CSE chemistry is in progress.

6.4 Paper IV

We have updated the chemical network of the CSE-chemistry model to include the ^{13}C and ^{18}O isotopes, all corresponding isotopologues, and their chemical reactions. Our new version includes 933 species and 15108 gas-phase reactions, whereas the old version involves 467 species and 6173 reactions. This enables us to probe the effects of UV chemistry on the isotopologue ratios of C- and O-bearing species.
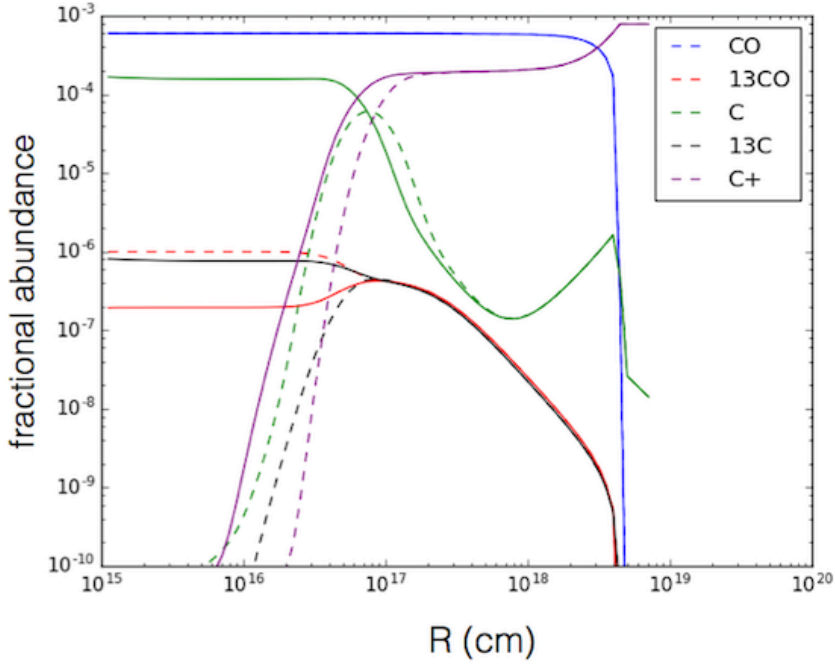
Figure 6.2: Fractional abundance distributions of CO, C, and C^+ without (dashed lines) and with (solid lines) an internal source of UV radiation.

In paper IV, we analyse the $^{12}CO/^{13}CO$ and $H^{12}CN/H^{13}CN$ isotopologue ratios in the CSEs of oxygen-rich and carbon-rich AGB stars with mass-loss rates $10^{-8} < \dot{M} < 10^{-4}$ $M_\odot$ yr^{-1}. We examine effects of varying the intensity of the interstellar radiation field and the gas kinetic temperature on the CO isotopologue distributions throughout the CSEs. We also perform a detailed radiative transfer (RT) modelling to derive the line intensity ratios of $I_{^{12}CO}/I_{^{13}CO}$ and $I_{H^{12}CN}/I_{H^{13}CN}$ for the same reference models in our chemical models for several rotational transitions to reasonably cover the inner and outer CSEs. We tested the influence of varying several input parameters in the RT modelling such as the dust condensation radius, the stellar temperature, the stellar luminosity, the CO abundance profile, and the gas expansion velocity on the CO line intensity ratio. Our preliminary results indicate that the CO abundance ratio can considerably deviate from its initial value depending on the initial condition. However, the HCN isotopologue ratio is stable throughout the CSEs of all tested models. This makes the circumstellar HCN isotopologue ratio a more reliable tracer of the photospheric C isotopic ratio.

Chapter 7

Summary and Outlook

In this thesis, we have studied the impact of UV radiation on the chemistry of the circumstellar envelopes (CSEs) surrounding evolved stars. This will provide a more complete picture of the chemical composition of CSEs and eventually of the interstellar medium.

We present the most updated calculations of the depth dependency of the CO photodissociation rate in the CSEs using the latest laboratory measurements. Our results show that the CO envelope size around AGB stars should be in fact smaller than the most commonly used radii in the literature. The improvement on the estimations of the CO photodissociation radii gained by our results improves the mass-loss rate estimates and subsequently the approximations of the amount of all other recycled material from AGB stars. We also present a comprehensive parameter study, where we examine variations of the CO envelope size by varying several CSE properties.

We implement an upgraded chemical network, in which we include the ^{13}C and ^{18}O isotopes, all the corresponding isotopologues, and their chemical reactions in the CSE-chemistry model. This enables us to trace variations of the isotopologue ratio of carbon- and oxygen-bearing circumstellar molecules throughout CSEs under varying initial conditions. We performed a parameter study for CO and HCN isotopologue ratios. Our findings show that the HCN isotopologue abundance ratio is stable throughout the CSEs, while the CO isotopologue ratio can considerably deviate from its initial value depending on the initial condition. Therefore, the HCN isotopologue ratio can be a more reliable tracer of the photospheric C isotopic ratio. For a carbon-rich AGB star, R Scl, we show that indeed the circumstellar $H^{12}CN/H^{12}CN$ ratio is a reliable tracer of the photospheric $^{12}C/^{13}C$ ratio by performing a detailed excitation analysis.

We present detection of the CI emission lines towards two UV bright AGB stars, omi Ceti and V Hya. CI is one of the main photodissociation product of parent species in the CSE around evolved stars.

To extend our sample of CI detected AGB stars, we applied for ALMA-ACA observations of CI towards another eight UV bright AGB stars. The observations have been partially carried out in Cycle 6 and will be continued in Cycle 7. For the same sample of AGB stars, we plan to apply for CII observations with SOFIA to more precisely constrain the C budget and CO photodissociation in these sources. Moreover, spatially resolved observations of the CI and CII may observationally distinguish the impact of various sources of UV radiation.

Furthermore, our future work will concentrate on implementation of an internal source of UV radiation in the CSE-chemistry model to analyze the impact of all potential sources of UV radiation more comprehensively. By doing so, we aim to quantify effects of internal sources of UV radiation. Moreover, it would be interesting to see whether the effects of different sources of UV radiation such as the interstellar radiation field, a hot binary companion, and stellar chromospheric activity on the CSE chemistry can be chemically distinguished.

To further our research, we also plan to perform a detailed radiative transfer analysis of our recent HCN observations to compare the line intensity ratio $I_{\mathrm{H^{12}CN}}/I_{\mathrm{H^{13}CN}}$ and the $I_{\mathrm{^{12}CO}}/I_{\mathrm{^{13}CO}}$ in the CSEs of a bigger sample of UV bright AGB stars.

Bibliography

Agúndez, M., Cernicharo, J., & Guélin, M. 2010, ApJ, 724, L133

Belitsky, V., Bylund, M., Desmaris, V., et al. 2018a, A&A, 611, A98

Belitsky, V., Lapkin, I., Fredrixon, M., et al. 2018b, A&A, 612, A23

Belitsky, V., Lapkin, I., Monje, R., et al. 2006, in Proc. SPIE, Vol. 6275, Society of Photo-Optical Instrumentation Engineers (SPIE) Conference Series, 62750G

Carpenter, K. G., Robinson, R. D., Johnson, H. R., et al. 1997, ApJ, 486, 457

Chapman, J. M., Sivagnanam, P., Cohen, R. J., & Le Squeren, A. M. 1994, MNRAS, 268, 475

Cherchneff, I. 2006, A&A, 456, 1001

Cherchneff, I. & Glassgold, A. E. 1993, ApJ, 419, L41

Danilovich, T., Bergman, P., Justtanont, K., et al. 2014, A&A, 569, A76

De Beck, E., Lombaert, R., Agúndez, M., et al. 2012, A&A, 539, A108

Draine, B. T. 1978, ApJS, 36, 595

Eaton, J. A. & Johnson, H. R. 1988, ApJ, 325, 355

Fong, D., Meixner, M., & Shah, R. Y. 2003, ApJ, 582, L39

Glassgold, A. E. & Huggins, P. J. 1986, ApJ, 306, 605

Goicoechea, J. R. & Le Bourlot, J. 2007, A&A, 467, 1

Greaves, J. S. & Holland, W. S. 1997, A&A, 327, 342

Groenewegen, M. A. T., Baas, F., de Jong, T., & Loup, C. 1996, A&A, 306, 241

Guélin, M., Lucas, R., & Neri, R. 1997, in IAU Symposium, Vol. 170, IAU Symposium, ed. W. B. Latter, S. J. E. Radford, P. R. Jewell, J. G. Mangum, & J. Bally, 359–366

Güsten, R., Nyman, L. Å., Schilke, P., et al. 2006, A&A, 454, L13

Habing, H. J. 1996, A&A Rev., 7, 97

Habing, H. J. & Olofsson, H., eds. 2003, Asymptotic giant branch stars

Hartmann, L., Dupree, A. K., & Raymond, J. C. 1982, ApJ, 252, 214

Herwig, F. 2005, ARA&A, 43, 435

Höfner, S. & Olofsson, H. 2018, A&A Rev., 26, 1

Johnson, H. R., Baumert, J. H., Querci, F., & Querci, M. 1986, ApJ, 311, 960

Judge, P. G. & Stencel, R. E. 1991, ApJ, 371, 357

Justtanont, K., Barlow, M. J., Blommaert, J., et al. 2015, A&A, 578, A115

Karakas, A. I. & Lattanzio, J. C. 2014, PASA, 31, e030

Khouri, T., de Koter, A., Decin, L., et al. 2014, A&A, 561, A5

Knapp, G. R., Crosas, M., Young, K., & Ivezić, Ž. 2000, ApJ, 534, 324

Lambert, D. L., Gustafsson, B., Eriksson, K., & Hinkle, K. H. 1986, ApJS, 62, 373

Leão, I. C., de Laverny, P., Mékarnia, D., de Medeiros, J. R., & Vandame, B. 2006, A&A, 455, 187

Le Bertre, T. 1997, A&A, 324, 1059

LeBlanc, F. 2010, An Introduction to Stellar Astrophysics (Wiley)

Lee, L. C. 1984, ApJ, 282, 172

Maercker, M., Mohamed, S., Vlemmings, W. H. T., et al. 2012, Nature, 490, 232

Maercker, M., Schöier, F. L., Olofsson, H., et al. 2009, A&A, 494, 243

Maercker, M., Schöier, F. L., Olofsson, H., Bergman, P., & Ramstedt, S. 2008, A&A, 479, 779

Maercker, M., Vlemmings, W. H. T., Brunner, M., et al. 2016, A&A, 586, A5

Mamon, G. A., Glassgold, A. E., & Huggins, P. J. 1988, ApJ, 328, 797

McDonald, I., Zijlstra, A. A., Lagadec, E., et al. 2015, MNRAS, 453, 4324

McElroy, D., Walsh, C., Markwick, A. J., et al. 2013, A&A, 550, A36

Meixner, M., Haas, M. R., Tielens, A. G. G. M., Erickson, E. F., & Werner, M. 1992, ApJ, 390, 499

Milam, S. N., Woolf, N. J., & Ziurys, L. M. 2009, ApJ, 690, 837

Millar, T. J. 2016, in Journal of Physics Conference Series, Vol. 728, Journal of Physics Conference Series, 052001

Montez, Jr., R., Ramstedt, S., Kastner, J. H., Vlemmings, W., & Sanchez, E. 2017, ApJ, 841, 33

Morris, M. & Jura, M. 1983, ApJ, 264, 546

Murthy, J. & Henry, R. C. 1995, ApJ, 448, 848

Ortiz, R. & Guerrero, M. A. 2016, MNRAS, 461, 3036

Querci, M. & Querci, F. 1985, A&A, 147, 121

Ramos-Medina, J., Sánchez Contreras, C., García-Lario, P., & da Silva Santos, J. M. 2018, A&A, 618, A171

Ramstedt, S., Mohamed, S., Vlemmings, W. H. T., et al. 2014, A&A, 570, L14

Ramstedt, S. & Olofsson, H. 2014, A&A, 566, A145

Ramstedt, S., Schöier, F. L., Olofsson, H., & Lundgren, A. A. 2008, A&A, 487, 645

Röllig, M. & Ossenkopf, V. 2013, A&A, 550, A56

Rybicki, G. B. & Hummer, D. G. 1991, A&A, 245, 171

Sahai, R., Findeisen, K., Gil de Paz, A., & Sánchez Contreras, C. 2008, ApJ, 689, 1274

Scharmer, G. B. 1981, ApJ, 249, 720

Schöier, F. L. & Olofsson, H. 2000, A&A, 359, 586

Schöier, F. L. & Olofsson, H. 2001, A&A, 368, 969

Schöier, F. L., Ryde, N., & Olofsson, H. 2002, A&A, 391, 577

Schrijver, C. J. 1995, A&A Rev., 6, 181

Van de Sande, M. & Millar, T. J. 2019, ApJ, 873, 36

Van de Sande, M., Sundqvist, J. O., Millar, T. J., et al. 2018, A&A, 616, A106

van Dishoeck, E. F. & Visser, R. 2011, arXiv e-prints, arXiv:1106.3917

Vassilev, V., Meledin, D., Lapkin, I., et al. 2008, A&A, 490, 1157

Visser, R., van Dishoeck, E. F., & Black, J. H. 2009, A&A, 503, 323

Vlemmings, W. H. T., Maercker, M., Lindqvist, M., et al. 2013, A&A, 556, L1

Watson, W. D., Anicich, V. G., & Huntress, Jr., W. T. 1976, ApJ, 205, L165

Weigelt, G., Balega, Y., Bloecker, T., et al. 1998, A&A, 333, L51